DANISH METEOROLOGICAL INSTITUTE

——— SCIENTIFIC REPORT ———

01-03

Calculation of wind gusts in DMI-HIRLAM

Niels Woetmann Nielsen

Claus Petersen

COPENHAGEN 2001

ISSN Nr. 0905-3263 (printed)
ISSN Nr. 1399-1949 (online)
ISBN-Nr. 87-7478-435-8

Calculation of wind gusts in DMI-HIRLAM

Niels Woetmann Nielsen and Claus Petersen
Danish Meteorological Institute, Copenhagen, Denmark

ooo ooo ooo

1. Introduction

Wind gusts are manifestations of turbulence. They are of concern mainly in the atmospheric boundary layer (ABL), and particularly in its surface layer because of their potential destructive effects on forests and constructions such as buildings and bridges. In general wind gusts may depend on local inhomogeneities as well as on horizontal gradients of meteorological variables like wind velocity, temperature and humidity. We will simplify things and only consider a horizontally homogeneous ABL. This is also consistent with the assumption of horizontal homogeneity of the turbulence within each grid column of the DMI-HIRLAM model.

The simplifications we have made imply that gusts generated by downdrafts in deep convection, that is convection involving a large fraction of the depth of the troposphere, are not considered. These gusts are of concern, but difficult to predict because of their association with deep convection.

In some applications it is assumed that the near surface wind gust G_u=$U + \delta u$, $\delta u \geq 0$, is simply proportional to the near surface mean wind speed U, i.e,

$$\frac{G_u}{U} = c(\geq 1). \tag{1}$$

This implies

$$\frac{\delta u}{u_{*0}} = (c-1) \cdot \frac{U}{u_{*0}} = (c-1) \cdot {C_D}^{-\frac{1}{2}}, \tag{2}$$

where $C_D = (u_{*0}/U)^2$ is the drag coefficient and u_{*0} is the surface friction velocity defined by $u_{*0} = \sqrt{\tau_0/\rho_0}$. In the latter expression τ_0 is the surface stress and ρ_0 is the air density at the surface. According to (2) the gust normalized by the surface friction velocity decreases with increasing surface drag C_D, and this is not what is intuitively expected. The expectation is that G_u is roughly proportional to the maximum mean wind speed in the ABL. The latter is not (or only weakly) dependent on the local surface drag. However, for a given horizontal pressure gradient force, the near surface mean wind speed decreases with increasing local surface drag, implying an increase of G_u/U in disagreement with (1) and (2). The dependence on surface roughness length can be taking into account by assigning different constants of proportionality (different c's) to typical roughness regimes. However, this generalization does not account for the dependence on static stability, indicated by (2).

Recently Brasseur (Brasseur, 2001) has developed a method, using mean turbulent kinetic energy (TKE) and buoyant energy within the ABL, to estimate the near surface wind gust. Upper and lower bounds for the wind gust are also determined. The upper bound is given by the maximum wind speed in the ABL and the lower bound is estimated from the local vertical turbulent kinetic energy and the buoyant energy.

In the present report we develop a wind gust formula based on similarity theory. The derivation of this formula is presented in section 2. In section 3 we compare wind gusts calculated from the formula with wind gust observations over the North Sea. A statistical test is performed in section 4. In this test we compare one year (2000) of forecasted wind gusts based on the derived formula with observed wind gusts at a selection of Danish synop stations. To keep forecast errors at a low level the comparison is restricted to 3 and 6 hourly DMI-HIRLAM forecast with the HIRLAM-E resolution (that is 0.15° horizontal resolution and 31 vertical levels). Predictions made by the gust factor formula are qualitatively validated on a severe storm case (3 December 1999) in section 5. In section 6 we compare the performance of our wind gust formula with the independent TKE method presented by Brasseur (Brasseur, 2001). Finally, section 7 contains discussion and conclusions.

2. Theory

In the horizontally homogeneous ABL we expect δu to depend on at least the kinematic stress (τ/ρ), the height z above the surface and the depth h of the ABL. The latter dependence is expected, because the turbulence usually becomes weak or dies out completely near the top of the ABL, implying $\delta u/U \approx 1$ at $z = h$. It should be noted that turbulence also may occur above the ABL, in particular in connection with jet streams. This type of turbulence, known as clear air turbulence (CAT), will not be considered here, although it is of concern for air traffic.

We will distinguish between two types of ABL's, the convective and the neutrally to stably stratified ABL.

2.1. The neutrally and stably stratified boundary layer

Here we will make the simplifying assumption that δu only depends on τ/ρ, z and h. Then, according to the Buckingham pi theorem, we obtain

$$\frac{\delta u}{u_*} = F_s\left(\frac{z}{h}\right), \tag{3}$$

where F_s is some as yet unknown function of z/h. Our aim here are to derive a gust formula applicable for the surface layer. The latter has typically a depth smaller than $0.1h$. We therefore expect F_s to be only weakly dependent on z/h in the surface layer. Furthermore, in the same layer we can regard the turbulence fluxes as being constants and equal to their surface values, denoted by subscript 0. In the surface layer (3) can therefore be approximated by

$$\frac{\delta u}{u_{*0}} = c_n, \tag{4}$$

where c_n is a constant, which in principle can be estimated from field measurements. Equation (4) can be written in the form

$$\frac{G_u}{U} = 1 + c_n \cdot \sqrt{C_D} \tag{5}$$

In the neutral surface layer the drag coefficient C_{Dn} is determined by

$$\sqrt{C_{Dn}} = \frac{k}{\ln z/z_{om}}, \tag{6}$$

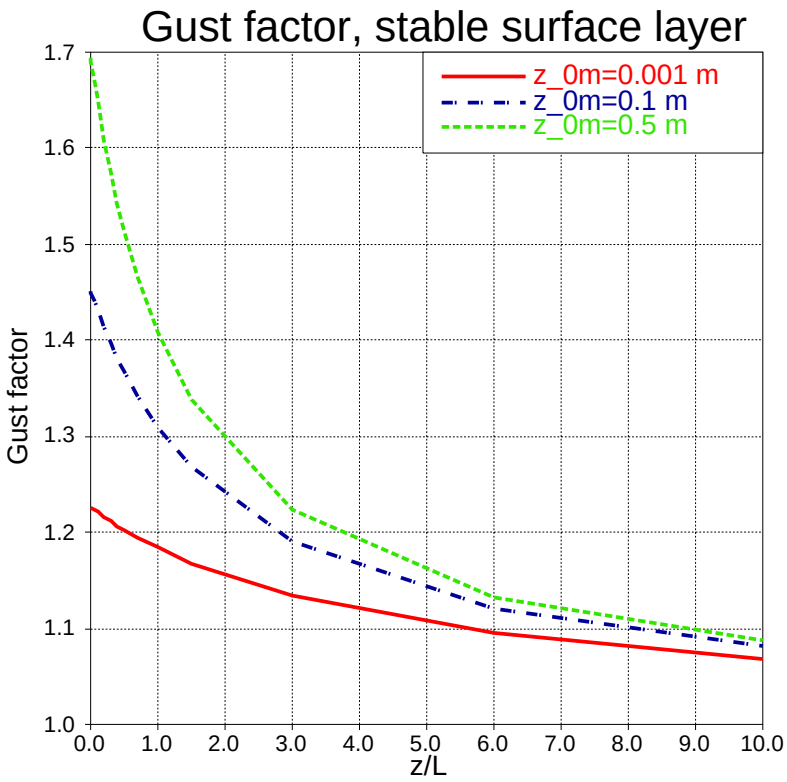

Figure 1: Variation of gust factor G_u/U with z/L in the stably stratified surface layer for the roughness lengths z_{0m}=0.001, 0.1 and 0.5 m. The gust factors are calculated with c_n=5.2 and S=0

where z_{0m} is the roughness length for momentum. In the stably stratified ABL C_{Ds} becomes a rather complex function of two more non-dimensional variables, respectively $\zeta = z/L$ and $S = N \cdot L/u_{*0}$, where L is the Monin-Obukhov stability length scale defined by

$$L = -(\tau_0/\rho_0)^{3/2} \cdot \left(\frac{k \cdot g \cdot H_{v0}}{\theta_0 c_p \rho_0} \right)^{-1} \tag{7}$$

and

$$S = \frac{NL}{u_{*0}}. \tag{8}$$

In the former equation H_{v0} is the surface virtual heat flux given by $H_{v0} \approx H_0 + 0.61 c_p \theta_{v0} E_0$, where H_0 is the surface sensible heat flux in $\mathrm{W\,m^{-2}}$ and E_0 is the surface moisture flux in $\mathrm{kg\,m^{-2}\,s^{-1}}$. In (8) $N = \sqrt{(g/\theta_v)\partial\theta_v/\partial z}$ is the Brunt-Vaisala frequency in the stably stratified free atmosphere above the stable ABL. According to the generalized similarity theory for the stably stratified surface layer (Zilitinkevich and Calanca, 2000) C_{Ds} takes the form

$$\sqrt{C_{Ds}} = k \cdot \left(\ln z/z_{0m} + C_{uL}(1 + \frac{C_{uN}}{C_{uL}} \cdot S) \cdot \frac{z}{L} \right)^{-1}, \tag{9}$$

where the C-constants in (9) have the values $C_{uL} = 2.1$ and $C_{uN} = 0.4$.

Equation (6) and (9) show that the gust factor G_u/U in the neutrally and stably stratified surface layer increases with increasing surface drag in agreement with expectation (based on the simple argument given previously). It follows from (9) that the gust

factor for a fixed value of S decreases with increasing stability (decreasing L). Note that for $S = 0$, (9) becomes identical with the wellknown form obtained from mid-latitude field experiments (e.g. the Kansas experiment, (Businger et al., 1971)). The variation of the gust factor (G_u/U) with z/L in the stably stratified surface layer is shown in Figure 1 for S=0 and for the roughness lengths z_{0m}=0.001, 0.1 and 0.5 m, respectively.

2.2. The convective boundary layer

In the convective ABL we expect δu to depend on the same parameters as in neutral and stable conditions. In addition to these parameters we also expect the buoyant production B_p of TKE, i.e. $B_p = -(g/\theta_0)H_{v0}/\rho_0 c_p$, to be a governing parameter.

We consider two limiting cases A and B. In A the buoyant production of TKE is significantly smaller than the shear production of TKE, and in B the reverse is true.

In case A we have $\delta u = f_A(u_{*0}, z, h)$ and by nondimensionalization

$$\frac{\delta u}{u_{*0}} = F_A\left(\frac{z}{h}\right) \approx F_A(0) = c_a. \tag{10}$$

In neutral (10) should match (4), implying $c_a = c_n$.

In case B we have $\delta u = f_A(B_p, z, h)$, where B_p is the buoyant production of TKE. We then obtain

$$\frac{\delta u}{w_*} = F_B\left(\frac{z}{h}\right) \approx F_B(0) = c_b, \tag{11}$$

where

$$w_* = (B_p \cdot h)^{1/3}, \tag{12}$$

is the convective velocity scale (Deardorff, 1972) and c_b is a constant. A simple combination of (10) and (11) yields

$$\frac{G_u}{U} = 1 + c_b\frac{w_*}{U} + c_n\frac{u_{*0}}{U}. \tag{13}$$

In case A, $u_{*0} >> w_*$, which means that (13) becomes approximately identical to (10). In case B, $w_* >> u_{*0}$, and in this case (13) becomes approximately identical to (11).

If we combine (13) with the corresponding equation valid for the neutrally and stably stratified surface layer we obtain

$$\frac{G_u}{U} = 1 + \gamma_u\left(c_b\frac{w_*}{U} + c_n\frac{u_{*0}}{U}\right) + \gamma_s c_n\frac{u_{*0}}{U}, \tag{14}$$

where $\gamma_u = 1 - \gamma_s$ and γ_s=1 and 0 in the stably and unstably stratified surface layer, respectively.

The values of the constants c_b and c_n are dependent on how the wind gust is defined, in such a way that their values increase if the time averaging period for the wind gust is shortened (Krayer and Marshall, 1992).

δu is proportional to the standard deviation (st.dev.) of the fluctuating horizontal wind velocity. Surface layer measurements (over flat homogeneous terrain) in neutral conditions (Garrat, 1992) indicate that $\sigma_u/u_{*0} \approx 2.4$ and $\sigma_v/u_{*0} \approx 1.9$. Here σ_u and σ_v are the st. dev. of the u and v components of the horizontal wind.

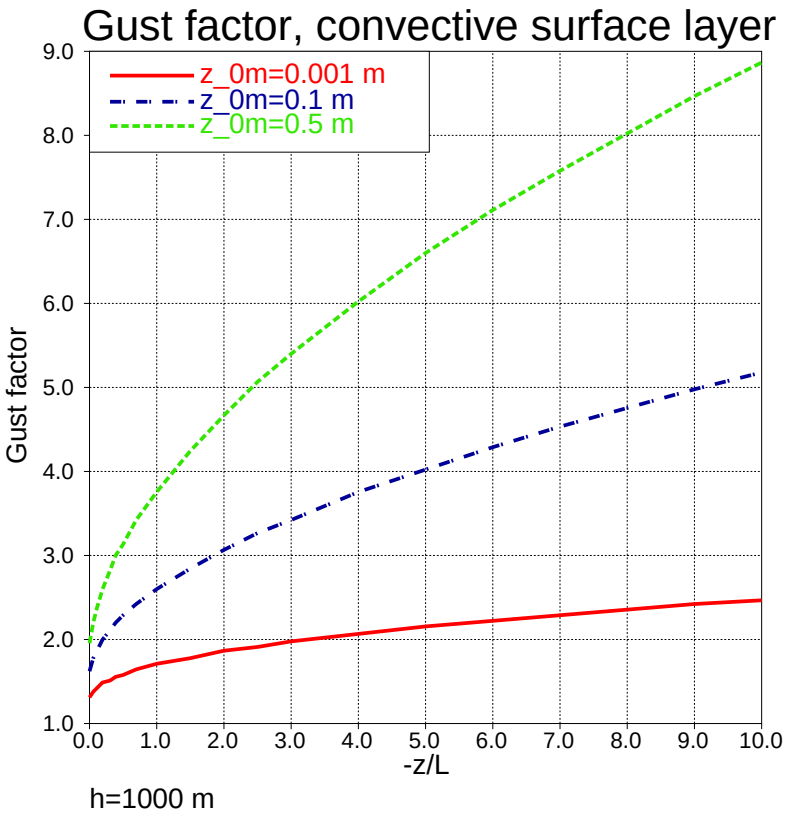

Figure 2: Variation of gust factor G_u/U with z/L in the unstably stratified surface layer for the roughness lengths z_{0m}=0.001, 0.1 and 0.5 m. The gust factors are calculated with c_n=5.2, c_b=1.44 and boundary layer height h=1000 m

If σ_U is defined by $\sigma_U = \sqrt{{\sigma_u}^2 + {\sigma_v}^2}$ it follows that $\sigma_U/u_{*0} \approx 3.06$. Similar measurements in convective conditions (Panofsky et al., 1977) show $\sigma_u/w_* \approx \sigma_v/w_* \approx 0.6$ and hence $\sigma_U/w_* \approx 0.85$. These results yield $c_b \approx c_t \cdot 0.85$ and $c_n \approx c_t \cdot 3.06$. The constant of proportionality, c_t, will be estimated statistically from observations and "predicted observations" obtained by applying (14). As a first guess we assume that c_t= 1.7, giving c_b=1.44 and c_n=5.20. The variation of the gust factor with z/L in the convective surface layer for a fixed boundary layer height h=1000 m is shown in Figure 2 for the roughness lengths z_{0m}=0.001, 0.1 and 0.5 m. Around neutral stratification the magnitude of the gust factor changes abruptly as the buoyancy production of TKE changes from a source to a sink term or vice versa. This is highlighted in Figure 3. Primarily due to non-stationarity and inhomogeneous surface conditions such as nonuniform surface temperature and soil wetness, neutral conditions in the ABL are rarely met. Even at high wind speeds the flow in the ABL will experience patches over which its surface layer static stability changes sign. A smoothing of the gust factor curves in near neutral stratification in such a way that the gust factors are increased and reduced in weakly stable and weakly unstable stratification, respectively, would attempt to take these effects into account. An example of such a smoothing is shown in Figure 4. In the latter the gust factor curve has been smoothed in the interval $z/L \in [-\epsilon, \epsilon]$ by applying the interpolation formula

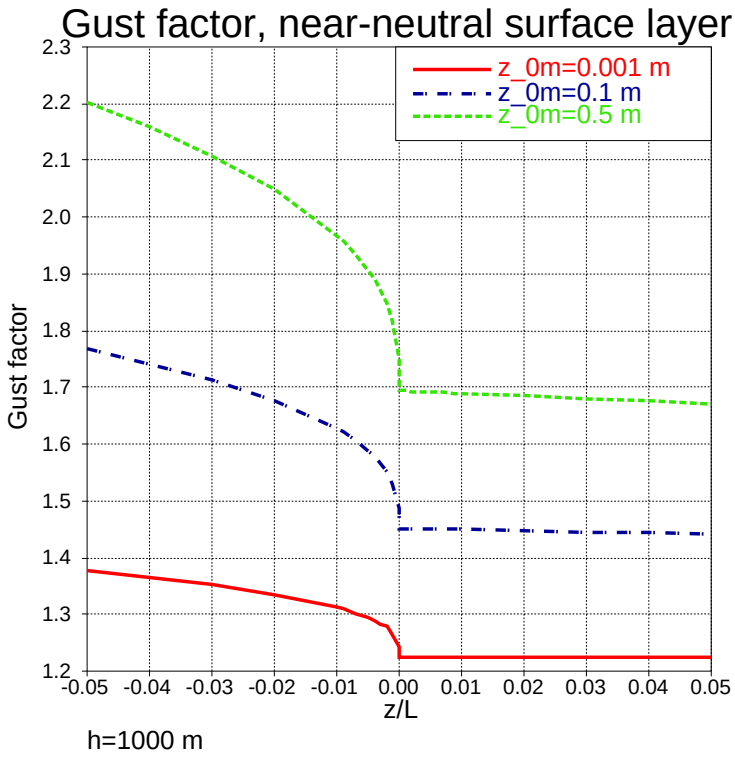

Figure 3: Variation of the gust factor G_u/U in the near-neutral surface layer for roughness lengths z_{0m}=0.001, 0.1 and 0.5 m. The gust factors are calculated with c_n=5.2, c_b=1.44, S=0 and h=1000 m

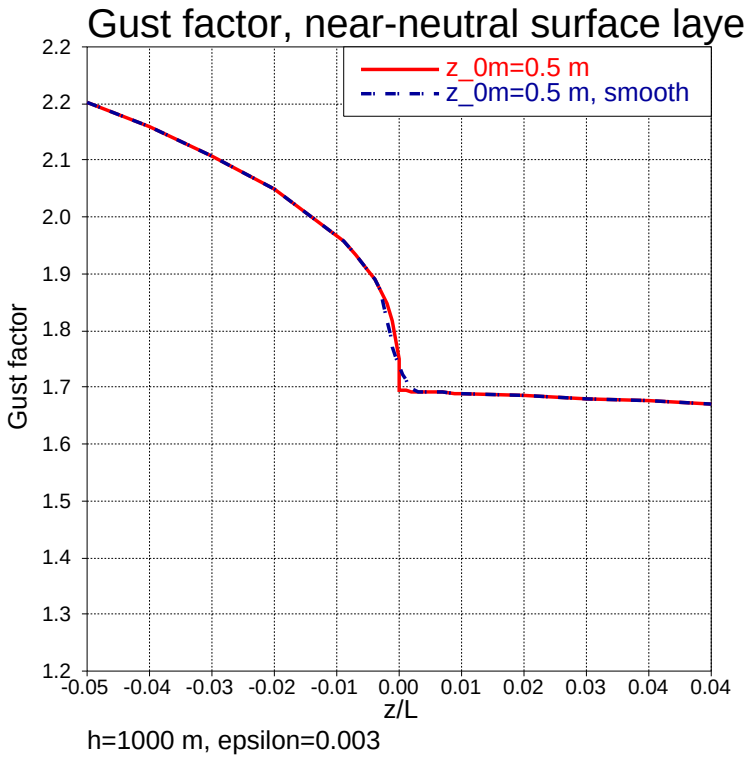

Figure 4: Variation of the gust factor G_u/U in the near-neutral surface layer for roughness length z_{0m}=0.5 m with and without smoothing in the interval $z/L \in$[-0.003,0.003], see text for details. The gust factors are calculated with c_n=5.2, c_b=1.44, S=0 and h=1000 m

$$\left(\frac{G_u}{U}\right)_{mod} = w_g \cdot \left(\frac{G_u}{U}\right)_{-\epsilon} + (1 - w_g) \cdot \left(\frac{G_u}{U}\right)_{\epsilon} \tag{15}$$

with

$$w_g = \left(\frac{\epsilon - z/L}{2 \cdot \epsilon}\right)^2. \tag{16}$$

In Figure 4, $(G_u/U)_{-\epsilon}$ and $(G_u/U)_{\epsilon}$ has been approximated by respectively

$$\left(\frac{G_u}{U}\right)_{-\epsilon} \approx c_b \cdot \left(\frac{1}{k} \cdot \frac{h}{z} \cdot \epsilon\right)^{1/3} + c_n \cdot \frac{k}{lnz/z_{0m} + \psi_{mu}(-\epsilon)} \tag{17}$$

and

$$\left(\frac{G_u}{U}\right)_{\epsilon} \approx c_n \cdot \frac{k}{lnz/z_{0m} + \psi_{ms}(\epsilon)}. \tag{18}$$

In (17) and (18), ψ_{mu} and ψ_{ms} is the non-logarithmic part of the vertically integrated dimensionless vertical wind shear in the unstably and stably stratified surface layer, respectively (Paulson, 1970).

3. Wind gust measurements at Horns Rev

An example of a time series of gust factors calculated from observed gusts (5 second means) and mean wind speed (averaged over 10 minutes) at 30 m height above mean sea level is shown in Figure 5. The observations represent conditions over coastal sea at Horns Rev southwest of Blåvand (station 6081 in Figure 10). The measurements were taken on a day (3 December 1999) with strong variations in mean wind speed due to the passage of an extremely intense extratropical cyclone, which has become known as the Denmark-cyclone. At 30 m the mean wind speed increased from below $10\,ms^{-1}$ in the morning to nearly $40\,ms^{-1}$ around 18 UTC. The corresponding variation in the 1 hour running mean wind gusts at the heights 15 m, 30 m and 62 m above mean sea level is shown in Figure 6.

Figure 5 shows considerable variability in the gust factor. In the early morning hours both observations and satellite images indicate shower activity over the eastern North Sea and Denmark. Therefore, it is likely that the gust factor peak values in the early period are associated with shower activity in combination with relatively low mean wind speeds. According to (14) the gust factor depends on both static stability, surface roughness length and height above the surface. With the assumption of neutral stratification, a sea surface roughness length $z_0 = 1\,\mathrm{mm}$ and c_n=5.2, the gust factors at the heights 15 m, 30 m and 62 m, calculated from (14), takes the values 1.216, 1.202 and 1.189, respectively. Figure 7 depicts differences between 1 hour running mean gust factors at 15 m and 62 m height and at 30 m and 62 m height obtained from observations. The calculated differences from (14), and with the assumptions given above, are respectively, 0.027 and 0.013. Figure 7 shows that only the latter number is in fair agreement with the measurements. The former number is an underestimation of the measured difference.

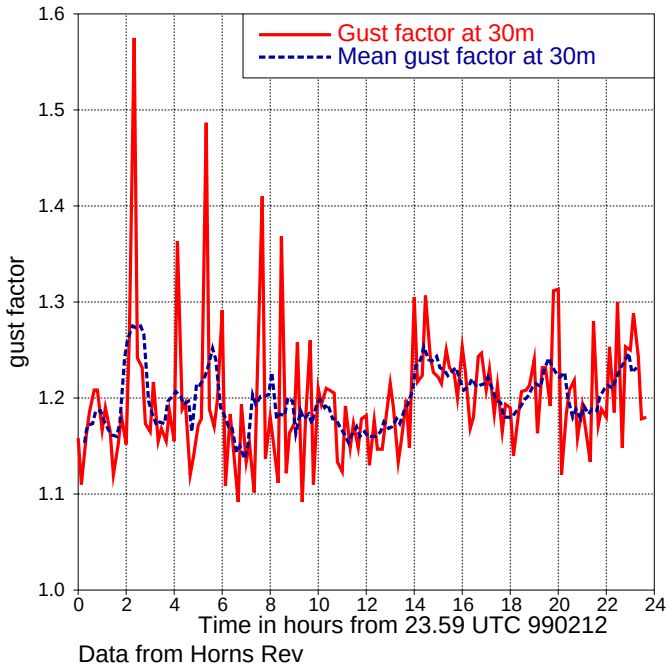

Figure 5: Wind gust factor (full) and 1 hour running mean gust factor (dashed) calculated from observed 30 m gusts (average over 5 seconds) and 30 m mean wind speed (10 minutes) at on 3 December 1999 Horns Rev in the North Sea southwest of Blåvand (station number 6081 in Figure 10).

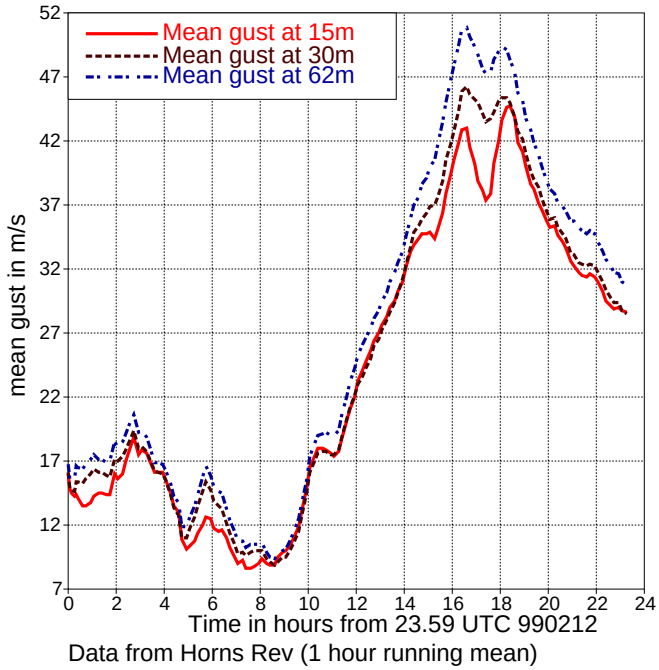

Figure 6: One hour running mean gusts on 3 December 1999 at Horns Rev in the North Sea southwest of Blåvand (station number 6081 in Figure 10).

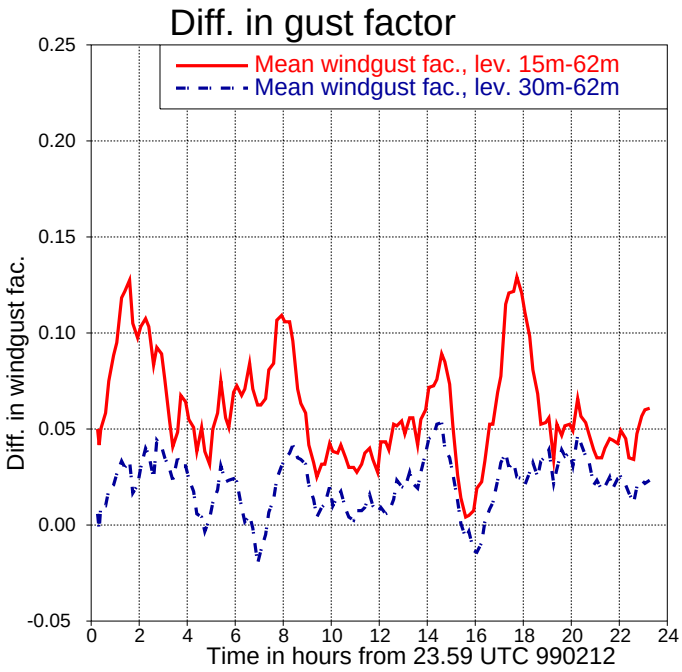

Figure 7: One hour running mean difference of the wind gust factor at heights 15 m and 62 m (full), and at heights 30 m and 62 m (dash dotted) on 3 December 1999 at Horns Rev in the North Sea southwest of Blåvand (station number 6081 in Figure 10).

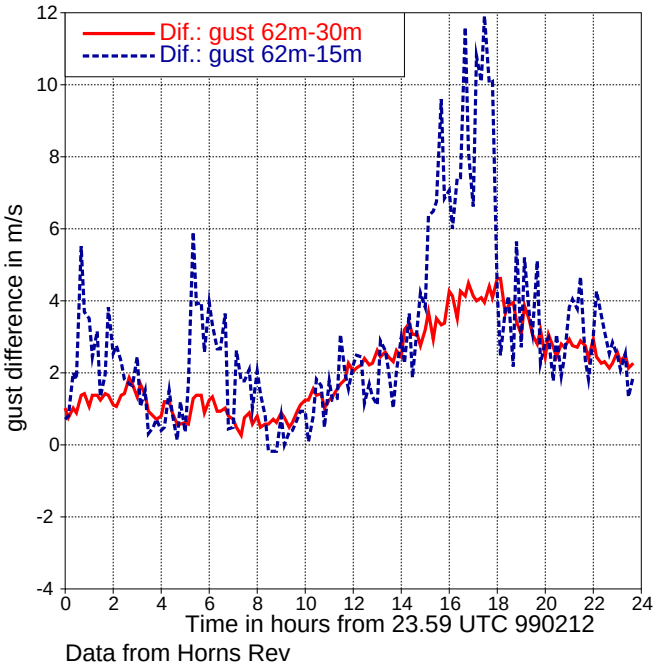

Figure 8: Difference in wind gust between heights 62 m and 15 m (dashed), and between heights 62 m and 30 m (full) on 3 December 1999 at Horns Rev in the North Sea southwest of Blåvand (station number 6081 in Figure 10).

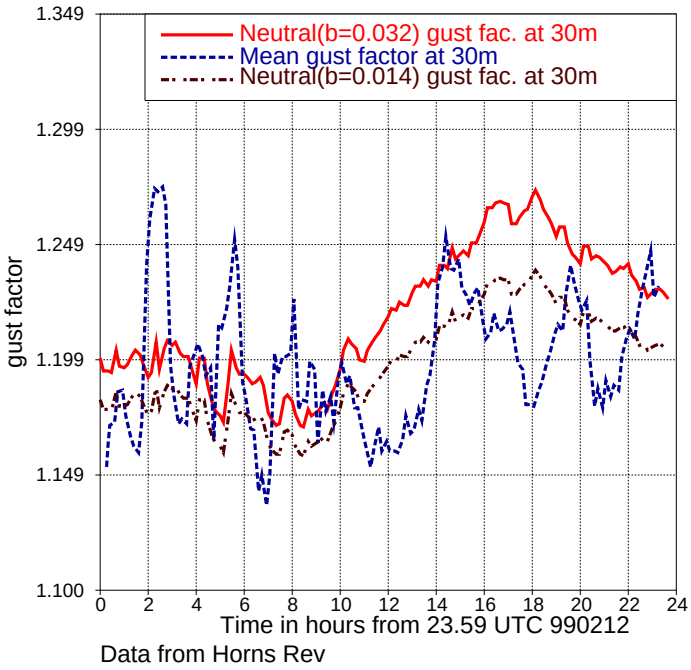

Figure 9: Observed 1 hour running mean gust factor (dashed) and hypothetical neutral gust factors with β=0.014 (dash-dotted) and β=0.032 (full) calculated from (20) using observed 30 m mean wind speeds at Horns Rev.

The gust differences in Figure 8 show that the gusts at 15 m are considerably damped in certain periods, indicating that the flow at this level is significantly perturbed by the sea waves. This may be one reason why the gust factors calculated from observations at this level generally are higher than expected from (14). In contrast the gust difference between the heights 62 m and 30 m is much smoother. Furthermore, the dashed curve in Figure 5 shows that the gust factor 1.201 obtained from (14) represents the data quite well. Both an increase in static stability and a decrease in z_0 will reduce the gust factor, while a decrease in static stability and an increase in z_0 has the opposite effect. Part of the variation in the gust factor and its 1 hour running mean is undoubtly due to variations in both static stability and surface roughness length.

An impression of the contribution from a variable z_0 to the observed variability in the gust factor is obtained from Figure 9. This figure shows, in addition to the 1 hour running mean gust factor at 30 m, two hypothetical gust factor curves. The latter curves are calculated from the observed mean wind speed at 30 m by assuming neutral stratification and using Charnock's relation

$$z_0 = \beta \frac{{u_*}^2}{g} \tag{19}$$

with β=0.032 and β=0.014, respectively. The resulting equation

$$F(u_*) = 2 \cdot u_* \ln \frac{u_c}{u_*} - k \cdot U = 0 \tag{20}$$

is solved iteratively by using the first guess u_*=0.04·U and in each iteration incrementing u_* by

$$\delta u_* = \left(-2 \cdot (\ln \frac{u_c}{u_*} - 1) \right)^{-1} \cdot F(u_*) \tag{21}$$

with the constraint $u_* + \delta u_* > 0$ or equivalently, in the first guess requiring that $u_* < 0.5 \cdot k \cdot U$. In (20) and (21) u_c is a Charnock wind speed defined by $u_c = \sqrt{z \cdot g \cdot \beta^{-1}}$. Note that $u_c(z_0) = u_*$. The iteration method is very fast. Applied to the data from Horns Rev it only requires 1 to 3 iterations to obtain the accuracy $|F(u_*)| < 10^{-5}$. Even the unrealistic first guess $u_* = U$ only requires 5 to 8 iterations to get an accuracy higher than 10^{-5}. The curve with β=0.014 appears to give a better fit to the observations (dashed curve in Figure 9) than the curve with β=0.032, in particular in the period with high wind speeds. Still, there are periods with considerable differences between the observations and the hypothetical curves. Variation in the surface layer static stability contributes to these differences, but its effect can not be easily quantified, because data about the surface layer static stability is not available. However, it is clear from Figures 1, 2 and 3 that unstable and stable stratification is associated respectively with an increase and a decrease in the gust factor.

The static stability also affects z_0 calculated by (19). At a given mean wind speed z_0 is higher/lower than its neutral value if the surface layer is unstably/stably stratified. This amplifies the deviation of the gust factor from its neutral value in both unstable or stable stratification.

The data in Figure 9 represents 3 frontal passages. The observations (sea level pressure, temperature, relative humidity and wind velocity) and satellite images show a warm front passage between 9 and 11 UTC, a cold front passage between 13 and 15 UTC and a bent-back warm front passage between 16 to 19 UTC. During the frontal passages the assumption of horizontal homogeneity is clearly violated, and the applicability of (14) in such conditions is questionable. It can be noted from Figure 9 that the gust factor decreases during the warm front passage and increases rapidly during the cold front passage. In the warm sector (from about 11 to 13 UTC) the gust factor is relatively low and increases at a rate corresponding to the hypothetical neutral curve with $\beta = 0.014$. In the warm sector the surface layer is likely to have a weak stable stratification, which is in accordance with the observed low gust factors. Likewise the air on the cold side of the cold front is likely to have a weak unstable stratification in accordance with the observed high gust factors. The bent-back warm frontal zone usually is stably stratified. Again, this is qualitatively in agreement with the observed variation of the gust factor from about 16 to 19 UTC. As the station enters the frontal zone the gust factor decreases, and, as it moves out again, the gust factor increases. It is not possible to draw any firm conclusion about the applicability of (14) based on the comparison with the Horns Rev data, although the major trends in the gust factor variability appears to be well captured by the formula. A more thorough statistically based validation is presented in the next section. In section 5 the Horns Rev data is further discussed in connection with a case study of the Denmark-cyclone.

4. Forecasted versus observed gusts

4.1. Wind gust observations

In the present study we will utilize wind gust measurements from Danish synop stations to validate the gust factor formula in (14). Traditionally, the 3 hourly (or sometimes 6 hourly) reports contain the maximum observed wind gust within the last 3 hours (occasionally 6 hours).

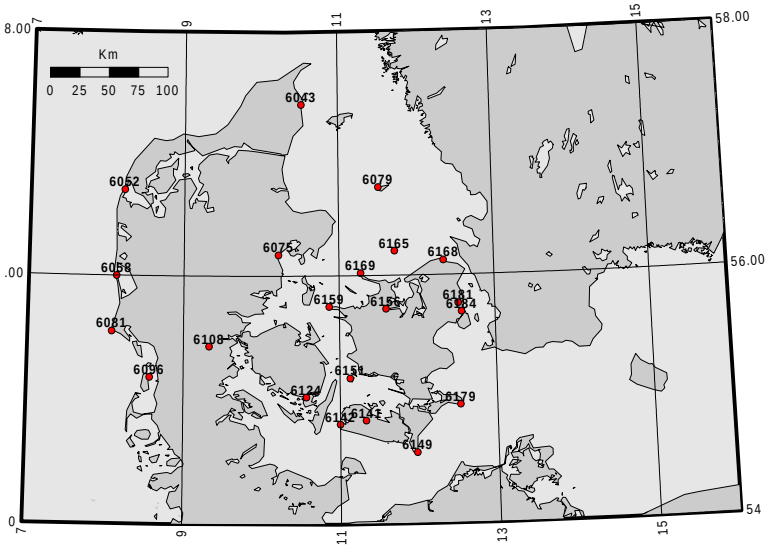

Figure 10: Location of Danish synop stations used in the present report.

These wind gusts are not well suited for a comparison with numerical model predicted wind gusts and are therefore not considered in this report. However, in the last few years wind gusts have also been reported every 10 minutes at a steadily growing number of Danish automatic weather stations. The wind gusts in these frequent reports are the maximum 3 second average wind speed measured within the last 10 minutes. Wind gusts below $10\,\mathrm{m\,s^{-1}}$ are usually not reported. The latter type of observed wind gusts are well suited for the present study. As 2000 so far has been the year with the largest number of automatic weather stations reporting wind gusts frequently, we have chosen this year for our study.

More specifically, the data used in this report is synop measurements at 3,6,15,18 UTC for all months in 2000 and from the automated Danish synop stations shown in Figure 10. Observations from 00 and 12 UTC are not utilized in the present study, because 3 and 6 hour forecasts were only run from initial hours 00 and 12 UTC. Some of the synop stations have been upgraded during the year and from these stations frequent wind gust observations have only been available from the date of the upgrading. Table 1 shows for year 2000 the monthly number of wind gust observations at each synop station.

4.2. The forecasted wind gust

The wind gust formula derived in section 2 has been implemented in DMI-HIRLAM-E. This model has a horizontal resolution of 0.15° and 31 vertical levels. Predicted wind gusts from the DMI-HIRLAM-E model have been compared with observations as described in section 4.1. To avoid resource demanding reruns of the DMI-HIRLAM-E forecasts the wind gusts in this study have been calculated in a post processing step described below. As the purpose of the comparison was to test the quality of the gust formula the forecast errors have been kept at a relatively low level by using no longer

than 6 hour old forecasts from the data archive at DMI. At this short range only 3 and 6 hour DMI-HIRLAM-E forecasts are available in the archive. Of these we have used forecasts from 00 and 12 UTC in the present study, which means that wind gust measurements from 21, 00, 09 and 12 UTC are not used. Again this choice was a compromise between what was desirable and the resources available for the study.

For the test of the gust formula it is important that the data used in the comparison contains the diurnal cycle of the static stability variation in the surface layer. This is achieved (to some extent) by utilizing forecasts from both 00 and 12 UTC. With the given constraint on resources the alternative choice would have been to utilize forecasts from 6 and 18 UTC, but this choice would require a rerun of these non-archived forecasts.

Table 1: Number of observations distributed at each month and synop stations. For location of synop station see Figure 10

STATION	JAN	FEB	MAR	APR	MAY	JUN	JUL	AUG	SEP	OKT	NOV	DEC	ALL
6141	6	3	2		3	2		1			1	1	19
6052												3	3
6142	4		1										5
6151	4		2					1				1	8
6124	2	2	8	1	3	3		1	4	8	2	5	39
6043	9	7	9	2	6	3	3	3	5	13	8	3	71
6081	10	5	5	1	1	1			2	5	3		33
6108	10	10	7	1	1	3	1	1	5	10	5	5	59
6181	15	17	12		10	5	1	4	7	9	5	3	88
6075	18	11	12		3	8	8	4	1	6		6	77
6165	5	4	4	1	2	2	2	2		6		2	30
6156	5	2	2	1	2	1				1		2	16
6184	21	9	16		8	6	1	3	2	9	3	6	84
6058	14	11	9		3	1	2	1		9	5	5	60
6149	2	3	4		5	2				5	1	1	23
6159			4					1		2	1		8
6168	12	17	11		6	8	3	5	2	9	4	6	83
6096	5	1				1				4	2		13
6079	3	1		1	1					2	1		9
6169	2		1		2					2	2	2	11
6179	11	9	16	1	1	6	2	1		2		3	52
TOTAL	158	112	125	9	57	52	23	28	28	102	43	54	791

4.3. Wind gust forecasts by post processing

Before calculating the wind gusts in a post processing step the necessary model data were interpolated to the synop locations shown in Figure 10. By applying this interpolation procedure it becomes a particular problem that several Danish synop stations are situated on islands or close to the sea. This means that the local roughness length at these station sites are not representative for the grid square averaged roughness lengths used in the model. Furthermore, the magnitude of roughness lengths in the model ought to depend on the wind direction with smaller values if the upwind fetch is predominantly over sea. This naturally contributes to scatter in plots of observed versus predicted wind speed. The uncertainty associated with the interpolation of fraction of land and roughness length from the model grid to the synop stations also contributes to the scatter. For each station the interpolated values of fraction of land and roughness length used in the wind gust calculation are shown in Table 2. The roughness length over land varies seasonally. Therefore both roughness lengths for January and June are shown in the table. It can be seen that the roughness lengths are higher in the growing season (June) than in winter (January).

Table 2: Model fraction of land, land roughness and sea roughness. Note that roughness is a function of time. Sea roughness is max. 0.002 m. The land roughness is an interpolated value to the synop station which underestimates the land roughness because of the low roughness over sea.

STATION	FRLAND	JANUARY	JUNE
06043	0.590	0.056	0.071
06052	0.336	0.030	0.035
06058	0.098	0.013	0.015
06075	0.563	0.170	0.183
06079	0.028	0.003	0.003
06081	0.254	0.063	0.075
06096	0.500	0.0156	0.025
06108	1.000	0.107	0.132
06124	0.622	0.114	0.133
06141	0.516	0.056	0.074
06149	0.271	0.036	0.045
06151	0.004	0.001	0.001
06156	0.877	0.133	0.156
06159	0.029	0.002	0.002
06165	0.000	0.001	0.001
06168	0.571	0.163	0.184
06169	0.007	0.001	0.001
06179	0.039	0.012	0.015
06181	0.623	0.576	0.592
06184	0.341	0.458	0.466
06142	0.197	0.017	0.024

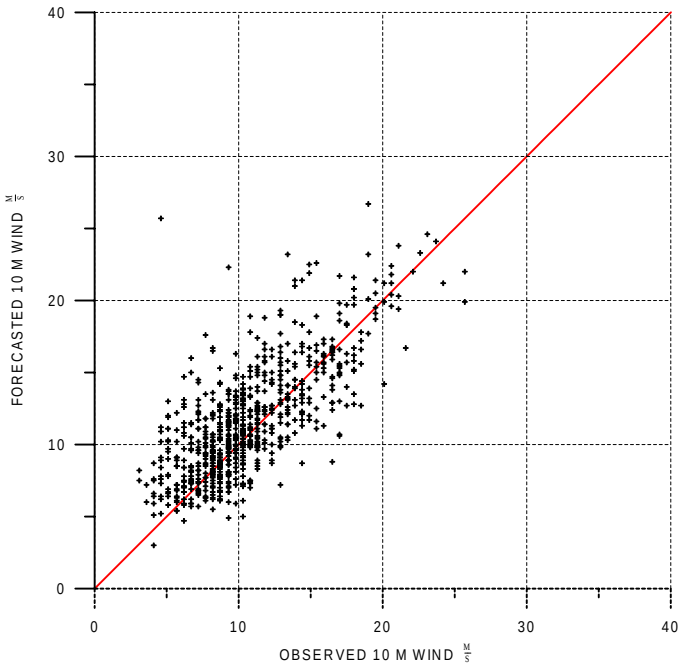

Figure 11: Observed versus forecasted 10 m land wind speed.

It is indicated by the roughness lengths in Table 2 that the interpolation procedure results in an underestimation of the roughness lengths at the observation site if the fraction of land is small. This is particularly apparent at the small island Hesselø (station 06165 in Table 2 and point 6165 in Figure 10). At this station the fraction of land is zero, and accordingly, the interpolated roughness length on this island has a value typical for rough sea.

The sensitivity of observed versus forecasted wind gust statistics on the roughness length used in the model calculations is investigated in the next subsection.

4.4. Comparison of observed and forecasted wind speed

The accuracy of the predicted wind gusts depends to some extend on the accuracy of the predicted mean wind speed. Therefore, the quality of the predicted 10m mean wind speeds will be investigated before we proceed to the evaluation of predicted 10m wind gusts against observed 10m wind gusts.

The scatter plots in Figures 11, 12 and 13 clearly show that the best result is obtained if the observed 10m wind speed is compared with the predicted 10m wind speed over fraction of land (the land wind speed in Figure 11). The forecasted 10m wind speed over fraction of sea (the sea wind speed) has a significant positive bias, as shown by Figure 12. Figure 13 shows that the positive bias is reduced somewhat if the observations are compared with forecasted 10m area averaged wind speeds (i.e. a fractional weighted average of the forecasted fraction of land and fraction of sea wind speeds).

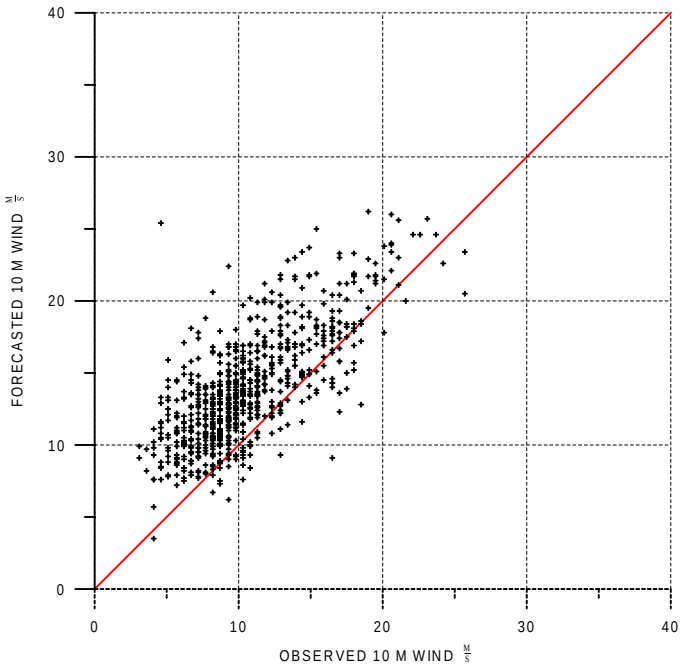

Figure 12: Observed versus forecasted 10 m sea wind speed.

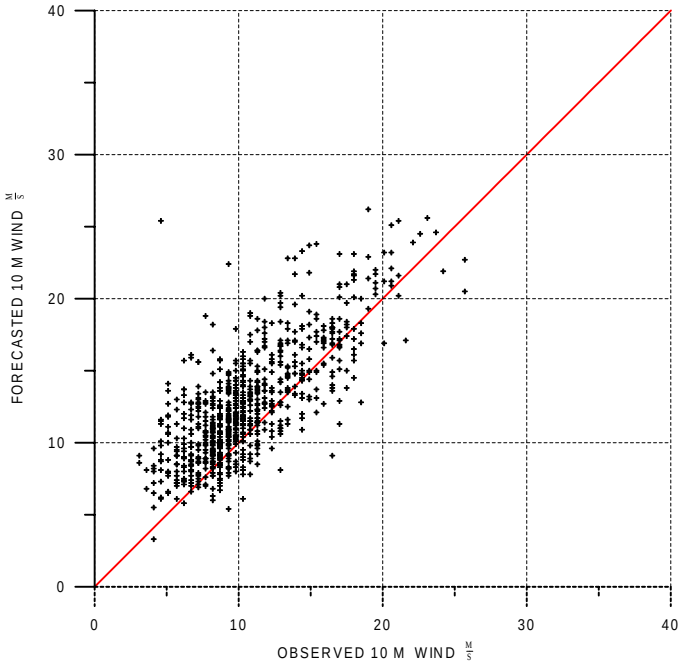

Figure 13: Observed versus forecasted 10 m area averaged average wind speed.

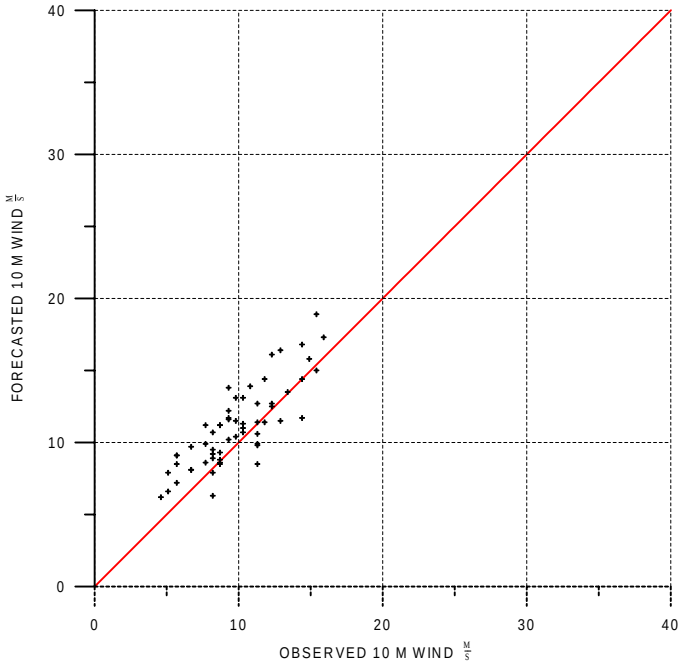

Figure 14: Observed versus forecasted 10 m land wind speed at Vamdrup (station number 06108)

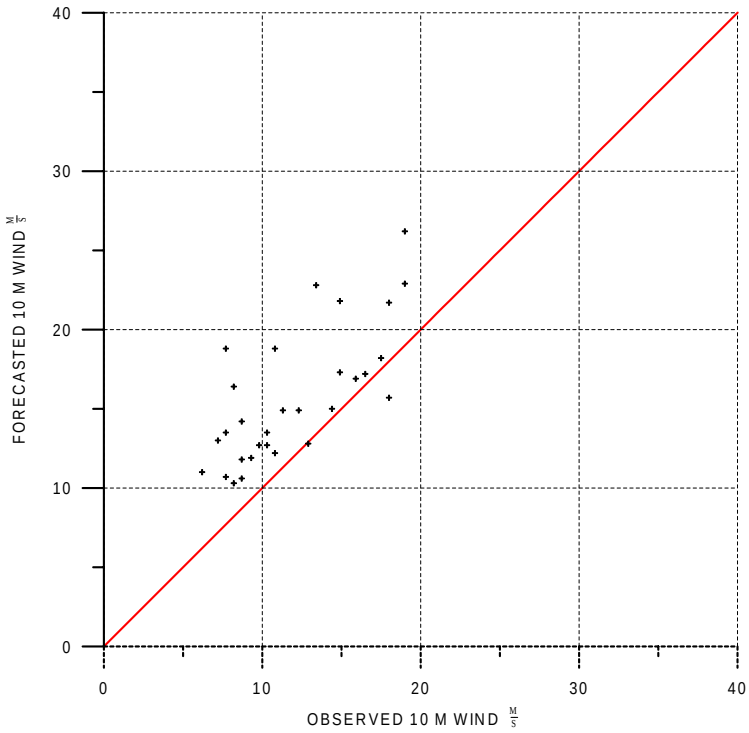

Figure 15: Observed versus forecasted 10 m sea wind speed at Hesselø (station number 06165).

Note that also the forecasted land wind speed (Figure 11) has a positive, but significantly smaller bias. The latter result is consistent with current operational obs-verification results (Nielsen and Amstrup, 2001).

According to Table 2 there is only one pure land station (06108 Vamdrup) and one pure sea station (06165 Hesselø) in the list. The scatter plot in Figures 14 confirms that the forecasted 10m wind at a land station with fraction of sea equal zero has a small positive bias. Figure 15 indicates that the local roughness length on a small island as Hesselø, having an interpolated fraction of land equal to zero, has a significant impact on the observed 10m wind speed. The use of a sea roughness length at such a location apparently results in a significant positive bias in the forecasted 10m wind speed. The same holds for other locations with a small interpolated fraction of land (for example station 06151, 06079 and 06159 in Table 2). It shows up as a clear positive bias in the predicted 10m area averaged wind speed in Figure 13.

4.5. Comparison of observed and predicted wind gust

The wind gust is expected to be less influenced by the local roughness length than the mean wind speed. This is confirmed by the scatter plots in Figure 16 and Figure 17. These figures show that it makes little difference whether the predicted gust is calculated over fraction of land, as in Figure 16, or it is calculated over fraction of sea, as in Figure 17.

It can be proved that $U_l/U_s < G_l/G_s$, where U is the mean wind speed and G the wind gust. Subscript l and s denote land and sea (or high and low surface roughness length), respectively. For the sake of simplicity we consider neutral stratification. From (5) follows

$$\frac{G_l}{G_s} = \frac{u_{*l}}{u_{*s}} \cdot \frac{c_n + k^{-1} \ln z/z_{0l}}{c_n + k^{-1} \ln z/z_{0s}} = f_a \cdot f_b, \tag{22}$$

in which f_a=u_{*l}/u_{*s} and f_b=$(c_n + k^{-1} \ln z/z_{0l})/(c_n + k^{-1} \ln z/z_{0s})$. From (6) and the definition of C_{Dn} we also have

$$\frac{U_l}{U_s} = \frac{u_{*l}}{u_{*s}} \cdot \frac{\ln z/z_{0l}}{\ln z/z_{0s}}. \tag{23}$$

Combining (22) and (23) yields

$$\frac{(U_l/U_s)}{(G_l/G_s)} = \frac{k \cdot c_n \cdot x_l + x_l \cdot x_s}{k \cdot c_n \cdot x_s + x_l \cdot x_s} < 1, \tag{24}$$

in which x_l=$\ln z/z_{0l}$ and x_s=$\ln z/z_{0s}$. A quantitative estimate can be obtained from a general form of the drag relations (Arya, 1977)

$$k \cdot U_r/u_* = \ln z_r/z_0 - A_r, \tag{25}$$

$$k \cdot V_r/u_* = -B_r \cdot signf, \tag{26}$$

in which U_r and V_r are the horizontal components (in the direction of surface shear and perpendicular to it, respectively) of mean velocity vector $\vec{V_r}$ at height z_r (above the matching layer). For a barotropic, neutrally stratified ABL (25) and (26) are replaced by

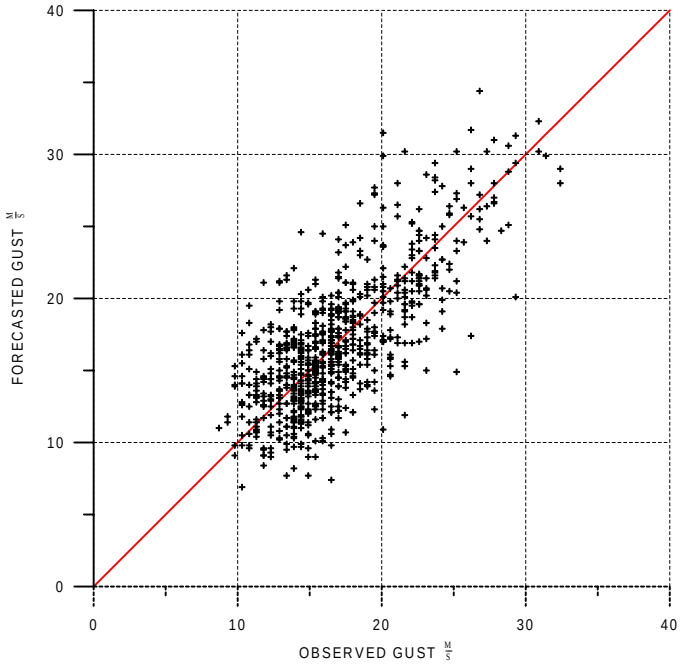

Figure 16: Observed gust versus forecasted gust at 10 m height based on forecasted wind speed over fraction of land.

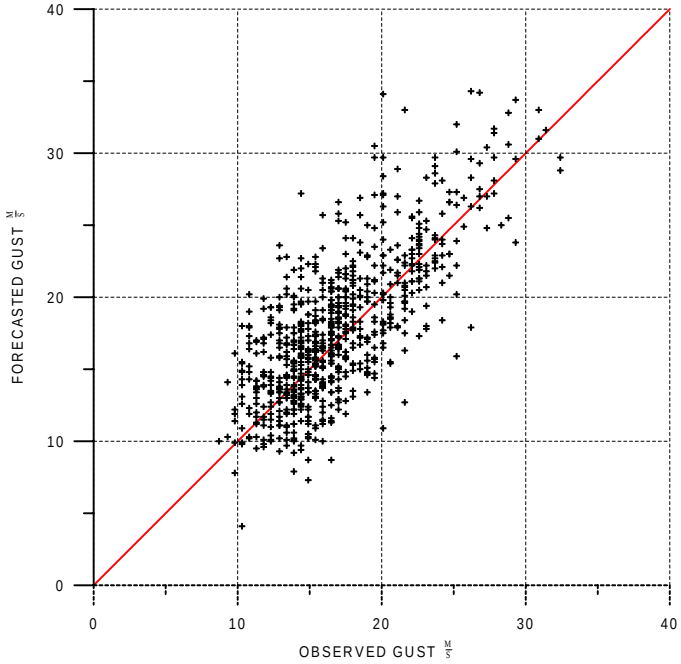

Figure 17: Observed gust versus forecasted gust at 10 m height based on forecasted wind speed over fraction of sea.

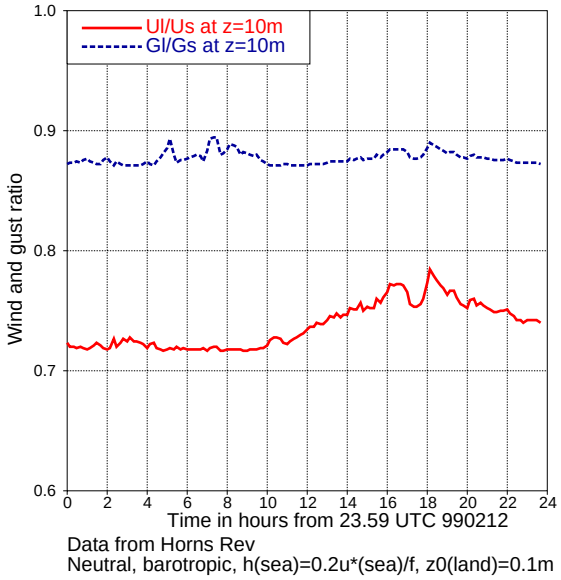

Figure 18: Ratio of 10 m land and sea wind speed (full) and ratio of the corresponding wind gusts (dashed) for a neutral, barotropic case. ABL height over sea is specified as $h_s = 0.2 \cdot u_{*s}/f$ and z_{0l} =0.1 m. Surface roughness length z_{0s} is calculated as for the dash-dotted curve in Figure 9.

$$k \cdot V_g/u_* = \left((\ln h/z_0 - A_N)^2 + {B_N}^2)\right)^{1/2}. \tag{27}$$

Here V_g is the geostrophic wind speed, $h = z_h$ is the height of the ABL and A_N, B_N are neutral, barotropic values of the similarity functions A_h, B_h. For $V_{gs} = V_{gl}$ we get from (27) and the definition of f_a

$$f_a = \left(\frac{(\ln h_s/z_{0s} - A_N)^2 + {B_N}^2}{(\ln h_l/z_{0l} - A_N)^2 + {B_N}^2} \right)^{1/2}, \tag{28}$$

in which h_l and h_s are the ABL heights over land and sea, respectively.

In neutral stratification the ABL height is often estimated as $h_N = c_h \cdot u_*/|f|$, where f is the Coriolis parameter and c_h a constant ($\approx$0.2). Figure 18 shows an example of hypothetical variations of G_l/G_s and U_l/U_s based on data from Horns Rev. The shown curves are calculated from (22), (23) and (28) by using $h_l = f_a \cdot h_s$, $h_s = 0.2 \cdot u_{*s}/|f|$, z_{0l}=0.1 m, $f = 1.2 \cdot 10^{-4}\, s^{-1}$, A_N=1.0, B_N=3.0 and c_h=0.2. The values of z_{0s} are identical with those calculated from (20) with β=0.014 (giving the dash-dotted gust factor curve in Figure 9). Equation (28) is written as

$$F(f_a) = {f_a}^2 \cdot C_l - C_s = 0, \tag{29}$$

in which $C_l = (\ln(f_a \cdot h_s/z_{0l}) - A_N)^2 + {B_N}^2$ and $C_s = (\ln(h_s/z_{0l}) - A_N)^2 + {B_N}^2$. This equation is solved iteratively from a first guess given by (28) with h_l replaced by h_s and by incrementing f_a by $\delta f_a = -F(f_a)/((1+2 \cdot C_l) \cdot f_a)$. Figure 18 clearly shows that the wind gust is less sensitive to local surface roughness length than the mean wind speed.

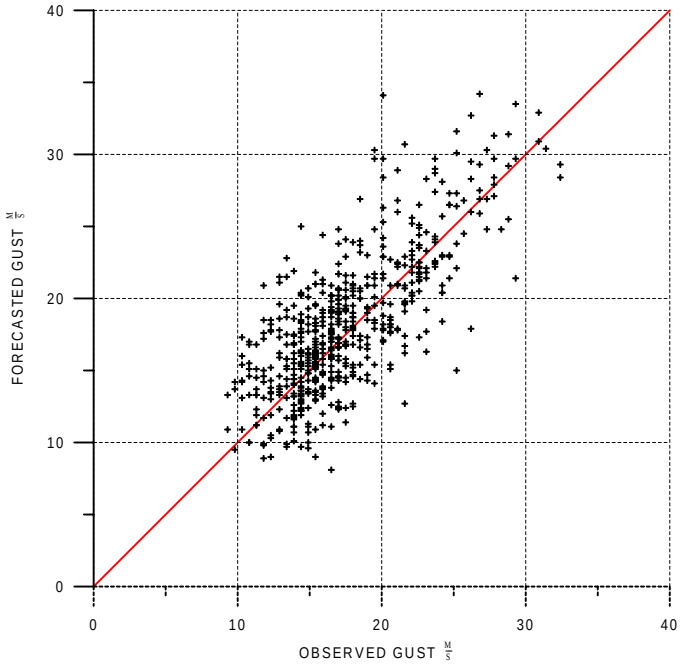

Figure 19: Observed gust versus forecasted gust at 10 m height for winter (October to March). Forecasted area averaged wind speed is used in the gust calculation.

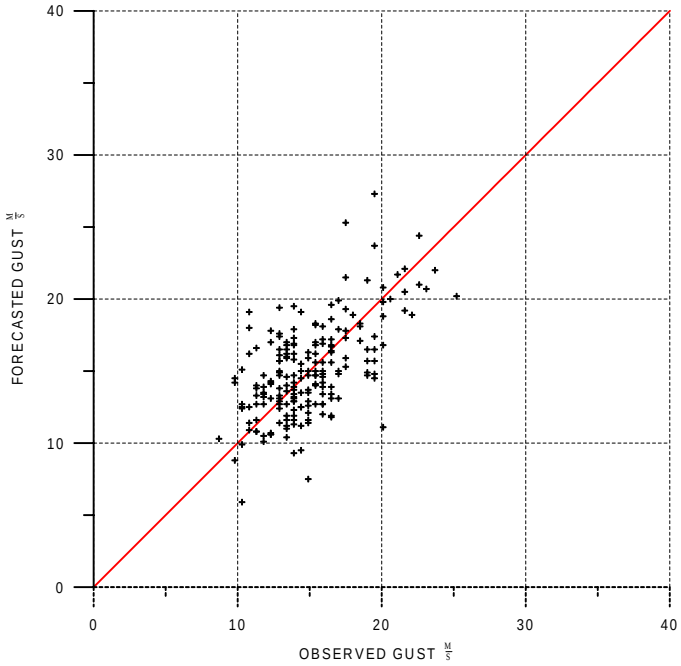

Figure 20: Observed gust versus forecasted gust at 10 m height for summer (April to September). Forecasted grid area averaged wind speed is used in the gust calculation.

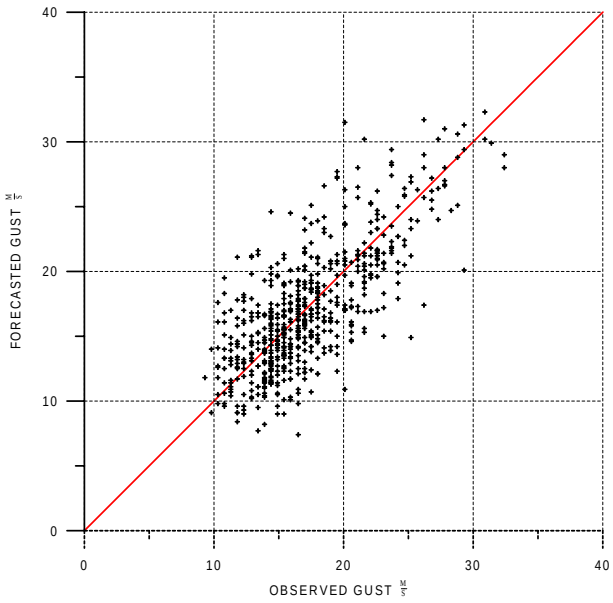

Figure 21: Observed gust versus forecasted gust at 10 m height for cases with stable stratification in the surface layer. Forecasted land wind speed is used in the gust calculation.

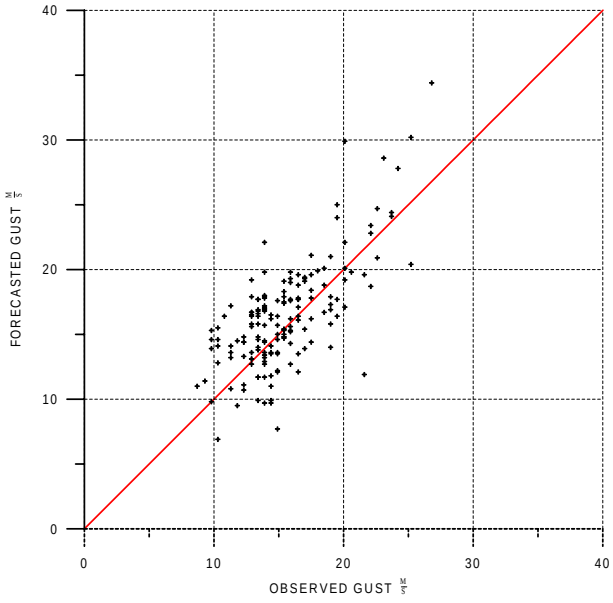

Figure 22: Observed gust versus forecasted gust at 10 m height for cases with unstable stratification in the surface layer. Forecasted land wind speed is used in the gust calculation.

The data has been split into winter (October to March) and summer (April to September) parts. Scatter diagrams for these half-year seasons are shown in Figure 19 and Figure 20, respectively. In both seasons the points are distributed around the line $y = x$ with only few predicted gusts deviating more than $5\,\mathrm{m\,s^{-1}}$ from the observed value. A majority of these points has a predicted gust larger than the observed, consistent with a positive bias of the predicted area averaged wind speed (see Figure 13). Comparison with Figure 16 indicates that the scatter is slightly reduced in Figures 19 and 20 if the forecasted area averaged wind speed is replaced by the forecasted land wind speed. The lower number of gust observations in the summer half-year is mainly a consequence of the climatological decrease in mean wind speed from winter to summer and the custom of not reporting wind gusts lower than $10\,\mathrm{m\,s^{-1}}$.

The gust factor calculated from (14) depends (among other parameters) on static stability in the surface layer. It is therefore relevant to consider separately data with predicted stable and unstable stratification. Scatter plots of these data are presented in Figure 21 and Figure 22, respectively. In both data sets a tendency for more points above than below $y = x$ is seen. This is consistent with a weak positive bias in land wind speed, as noted in subsection 4.4.

4.6. Gust factors

The observed 10 m gust factor versus observed 10 m mean wind speed for the data applied in the present study is shown in Figure 23. Regardless of the considerable scatter the figure unveils a clear nonlinear relationship between mean wind speed and gust factor. Both variation in stability, surface roughness length and boundary layer height contributes to the scatter. It is believed that the scatter is considerably reduced if the gust factor at each observation site is plotted as function of the stability parameter z/L_v, where L_v is defined by (7). We are unable to do this, because of lacking information about static stability. However, due to the similarity between Figure 23 and the corresponding Figure 24, showing forecasted gust factor (based on predicted land wind speed) versus observed land wind speed, we can indirectly show that a plot of observed gust factor versus observed z/L_v is likely to contain less scatter. Before doing this it should be noted (in connection with the intercomparison of Figure 23 and Figure 24) that observed wind gusts below $10\,\mathrm{m\,s^{-1}}$ are only occasionally reported. There is no such constraint in the forecasts. Consequently, the number of observed gust factors smaller than $10/U$ is lower than the corresponding number of predicted gust factors. It should also be noted that the forecasted gust factors (using forecasted sea wind speed) plotted versus observed $10\,m$ wind speed, shown in Figure 25, and representing conditions over sea, has much less similarity with Figure 23.

Figure 26 shows forecasted gust factor as function of forecasted z/L_v for Hesselø (06165), Møn (06179) and Vamdrup (06108). The gust factors for each station follow curves similar to those in Figure 3. The scatter seen in Figure 26 on the stable side ($z/L_v > 0$) is due to the seasonal variation of z_{0l} (stations 6108 and 6179) and the variation of z_{0s} with wind speed (stations 6179 and 6165). The scatter on the unstable side ($z/L_v < 0$) is due both to variations in surface roughness length and ABL height.

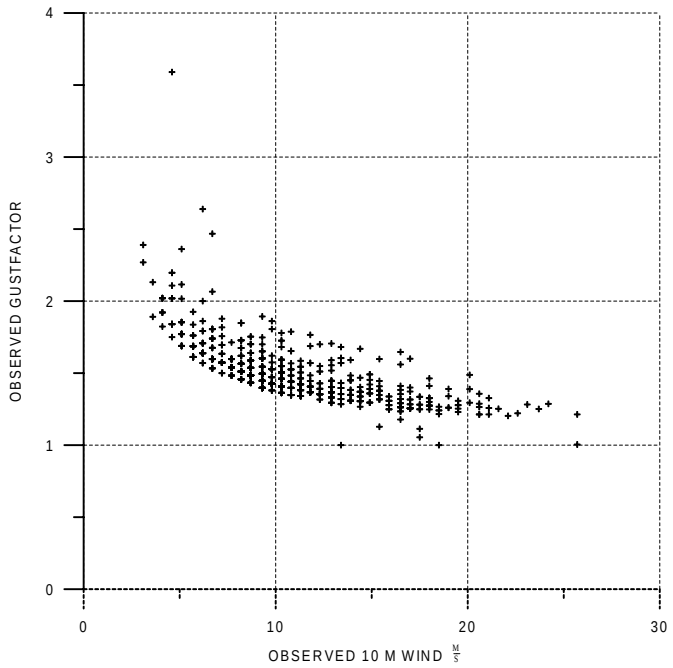

Figure 23: Observed gust factor G_u/U versus observed 10 m wind speed.

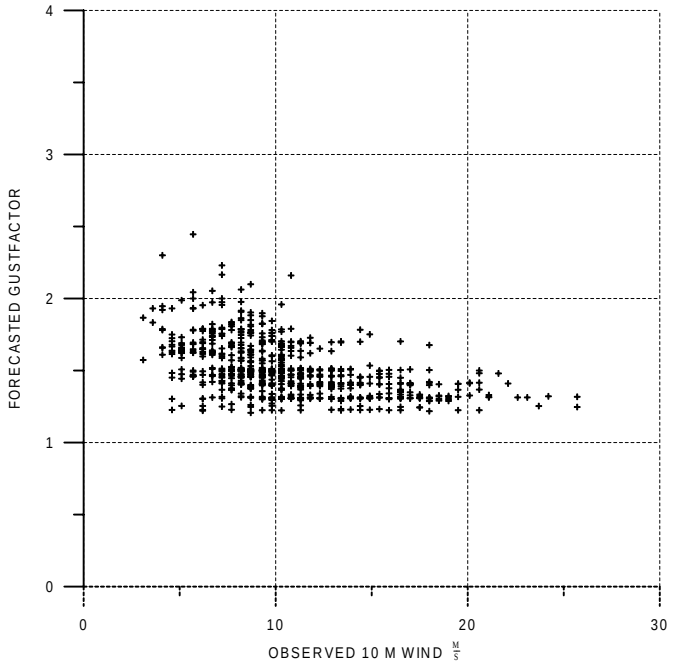

Figure 24: Forecasted 'land' gust factor G_u/U versus observed 10 m wind speed. Forecasted area averaged wind speed is used in the gust factor calculation.

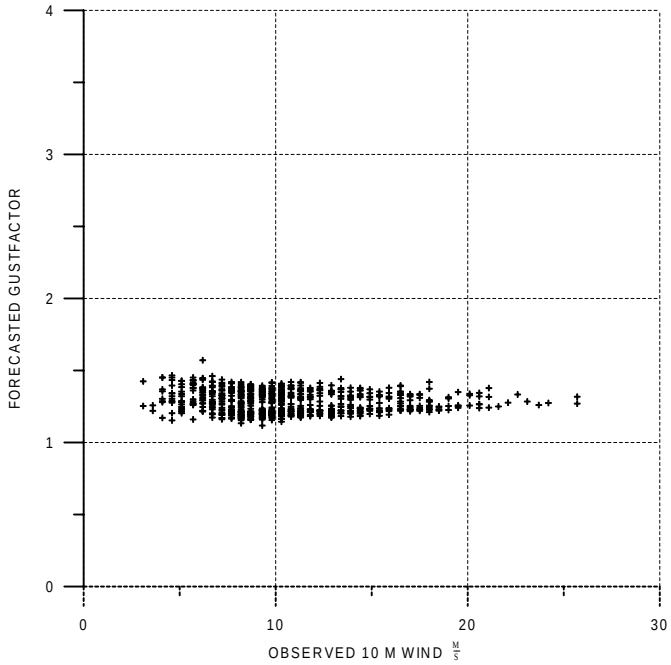

Figure 25: Forecasted 'sea'gust factor G_u/U versus observed 10 m wind speed. Forecasted sea wind speed is used in the gust factor calculation.

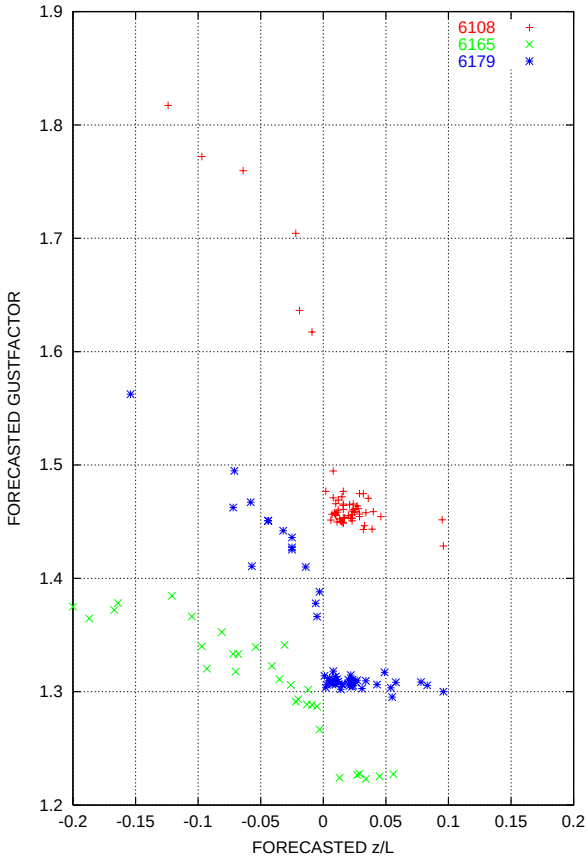

Figure 26: Forecasted 10 m gust factor versus $10/L_v$ for Hesselø (6165), Møn (6179) and Vamdrup (6108). Forecasted area averaged wind speed is used in the gust factor calculation

It is demonstrated by Figure 26 that a given mean wind speed, occurring at different stabilities, different surface roughness lengths and (in case of unstable stratification) at different ABL heights leads to scatter in the forecasted and observed gust factor plotted versus mean wind speed. Therefore, it is plausible that this explains a major part of the scatter in Figure 23 and Figure 24.

5. A case study

The statistical validation of the predicted wind gusts calculated from (14), presented in subsections 4.5 and 4.6, indicates that the wind gust is predicted with approximately the same accuracy as the 10 m wind speed. The present validation therefore indicates that the first guess c_t=1.7, giving c_n=5.20 and c_b=1.44 (see section 2.2), is a realistic choice. However, the validation data set is limited, and a future adjustment of c_t can not be excluded as more validation data becomes available.

It has been shown so far that (14) behaves satisfactorily in a statistical sense. The case study presented below also demonstrates its potential in individual cases. We have selected the Denmark-cyclone case (3 December 1999) for three reasons. First of all, from this case we have high quality wind gust measurements over sea. These measurements have been analyzed in some detail in section 3. Secondly, extreme wind gusts of about $100\,knots$ were recorded at a few locations along the southern part of the Danish North Sea coast. Furthermore, in association with passages of frontal bands (a warm front followed by a cold front, which again was followed by a bent-back warm front) both stably and unstably stratified ABL's become represented in this case. Thirdly, the Danish Meteorological Institute (DMI) has made a quite accurate (non-operational) forecast of this storm 36 hours in advance. This forecast has been rerun with unchanged resolution (i.e., 0.15° and 50 levels) on a sub domain centered over the North Sea for a 5 hour period beginning at 09 UTC on 3 December with the gust factor code implemented, and applying hourly updated boundary fields from the original run. The difference in $10\,m$ wind speed between the rerun and the original run has been checked and found to be less than $1\,\mathrm{m\,s^{-1}}$.

Figure 27 shows for the Denmark-cyclone case a 24 hour forecast of wind gust and gust factor valid for 12 UTC on 3 December 1999. The sharp horizontal gradient in the gust factor field (extending from the central North Sea to the west coast of Jutland) coincides with the surface warm frontal zone, while the somewhat weaker gradient extending from the central North Sea to East Anglia coincides with the surface cold frontal zone. It can be seen that a maximum in wind gust is located in a low level jet, blowing from the cold air north of the surface warm front, curving cyclonically around the cyclone center (southwest of the junction between the surface warm and cold front) and behind the surface cold front flaring out in a broad stream with maximum wind gusts between 70 and 80 knots.

The surface frontal structure of the cyclone is seen even more clearly in the convective velocity scale (w_*) and the turbulent surface sensible heat flux depicted in Figure 28. According to this figure w_* attains a maximum of more than $3\,\mathrm{m\,s^{-1}}$ in the low level jet (the cold conveyor belt (Browning, 1990)) on the cold side of the surface warm front and its backward extension into a developing bent-back warm front.

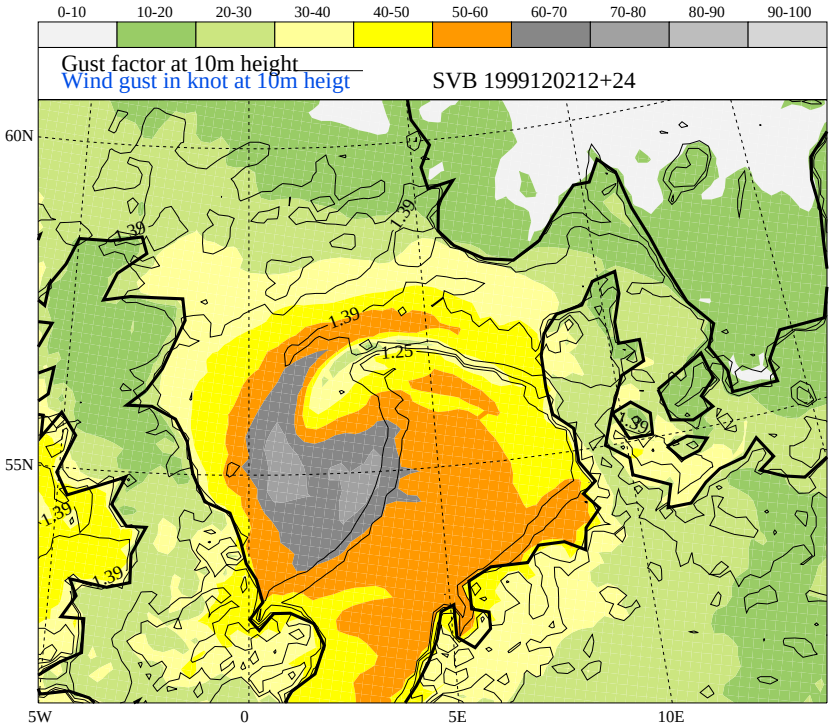

Figure 27: 24 hour forecast of wind gust (shading in intervals of 10 *knots*) and gust factor (full curves, only contours 1.2, 1.25, 1.3, 1.4 and 1.5 are drawn) valid at 12 UTC on 3 December 1999.

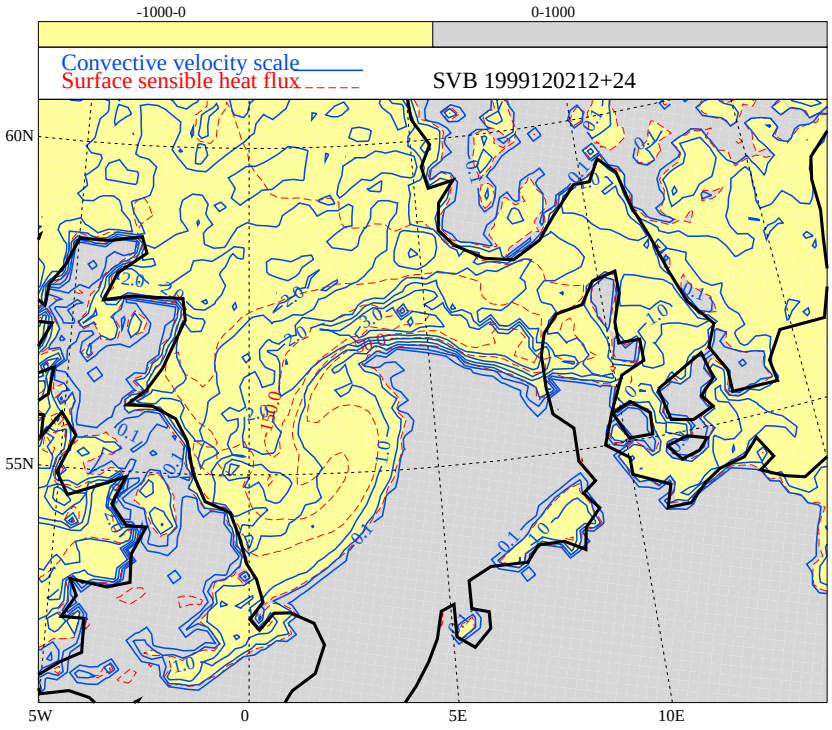

Figure 28: 24 hour forecast of surface sensible heat in $w\,m^{-2}$ (dashed, with contour interval $50\,\mathrm{W\,m^{-2}}$ and shading for downward flux) and convective velocity scale in $\mathrm{m\,s^{-1}}$ (full, with contours 0.1 and $0.5\,\mathrm{m\,s^{-1}}$ and thereafter every $0.5\,\mathrm{m\,s^{-1}}$) valid at 12 UTC on 3 December 1999.

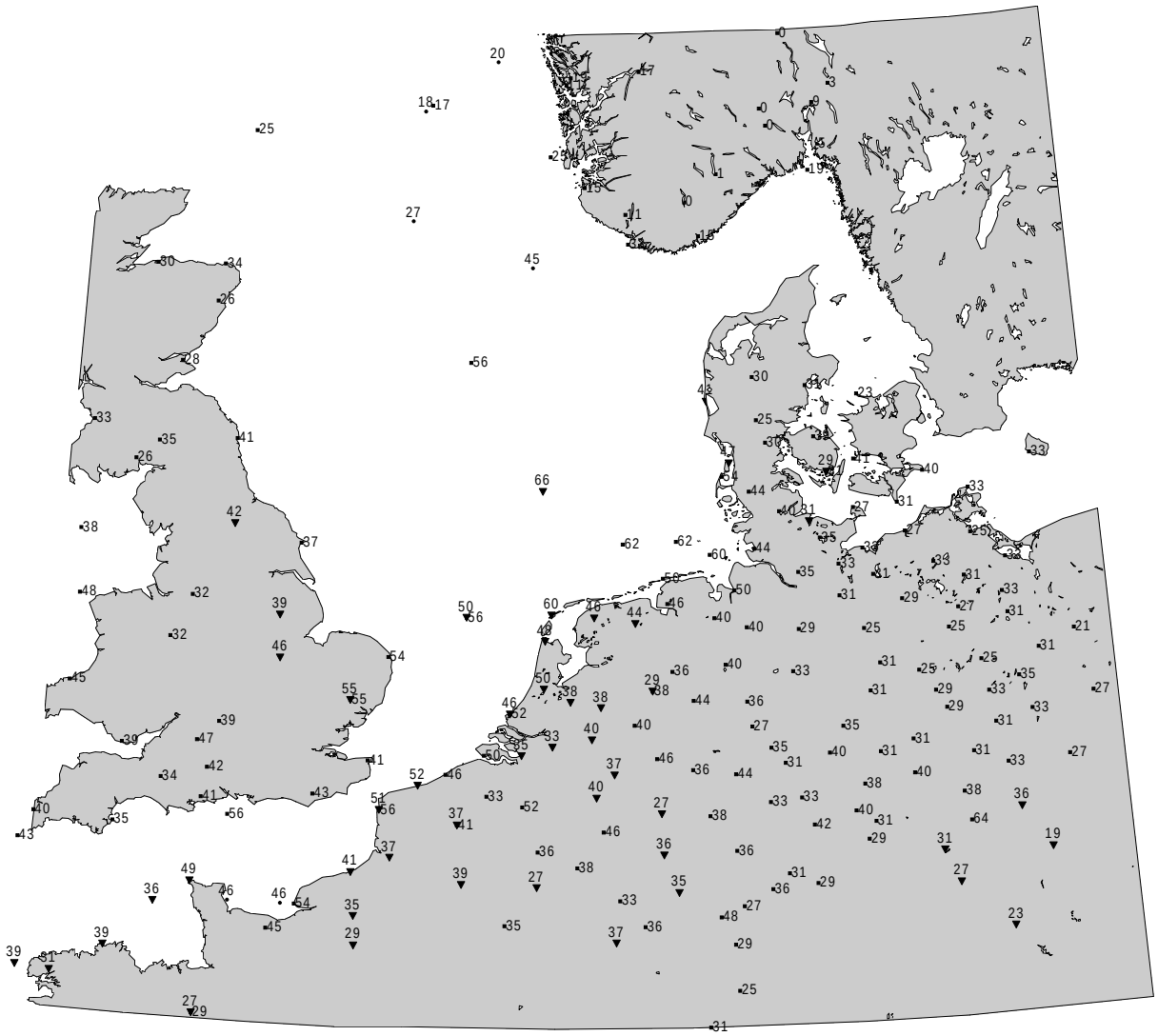

Figure 29: Wind gust observations in knots at 12 UTC on 3 December 1999. Stations reporting gusts every 10 minutes (code 910, black triangles), stations reporting gusts every 3 or 6 hours (code 911, black squares) and ship reports (black dots).

Not surprisingly, the regions with large w_* coincide with regions of large negative (upward) surface sensible heat flux ($<$ -150 w m^{-2}). In the forecast the warm sector of the cyclone is stably stratified with a positive sensible heat flux and (over sea) a negative latent heat flux (not shown). As the zero contour for w_* coincides with the zero contour for the surface virtual heat flux H_{v0} (defined in subsection 2.1) the contour w_*=0.1 m^{-2} in Figure 28 becomes located in the shaded region with positive (downward) sensible heat flux.

According to Figures 27 and 28 the horizontal gradient of the 10 m gust factor is mainly a result of the variation in surface layer static stability in terms of z/L_v and to a lesser degree due to variation in z_{0s}. According to Figure 9 the latter contributes to the gust factor variation at 30 m height by no more than 0.05. Over the North Sea the predicted 10 m gust factor is typical between 1.22 and 1.24 in the stably stratified warm sector of the cyclone, while peak values of more than 1.40 are predicted in the unstably stratified cold conveyor belt. The prediction is seen to be in qualitative agreement with the observations at Horns Rev discussed in section 3. Furthermore, the predicted wind gusts in Figure 27 are in overall good agreement with the verifying observations presented in Figure 29.

6. Comparison of wind gusts predicted by two alternative methods

In this section we compare results from the similarity-method (14) developed and tested in the present report with another recently developed and conceptually different TKE-method (Brasseur, 2001). As TKE is a prognostic variable in DMI-HIRLAM ((Cuxart et al., 1995) and (Sass et al., 2000)) this comparison can be done without big efforts.

In the TKE-method the wind gusts are estimated by assuming that a parcel flowing at a given height will be able to reach the surface if the mean TKE of large turbulent eddies is greater than the buoyant energy between the surface and the parcel height. This condition takes the mathematical form

$$\frac{1}{z_p} \cdot \int_0^{z_p} E(z) \cdot dz \geq \int_0^{z_p} g \cdot \frac{\Delta\theta_v(z)}{\theta_v(z)} \cdot dz, \tag{30}$$

where $E(z)$ is the local TKE, z_p is the height of the considered parcel, g is gravity, $\theta_v(z)$ is the virtual potential temperature and $\Delta\theta_v(z)$ is its difference across a given layer centered at z. A parcel from level z_p reaching the surface arrives with the wind speed $\sqrt{U^2(z_p) + V^2(z_p)}$. Parcels from different levels arrive at the surface with different wind speeds. The wind gust W_g is therefore estimated by

$$W_g = max[\sqrt{U^2(z_p) + V^2(z_p)}], \tag{31}$$

for z_p satisfying (30). Figure 30 and Figure 31 show that both methods give acceptable results, but the tendency for the TKE-method (Figure 31) to predict too high wind gusts, in particular at high gust speeds, should be noted. It has not been explored whether this trend can be explained by the assumptions leading to (30) or it is a result of the applied TKE parameterization scheme.

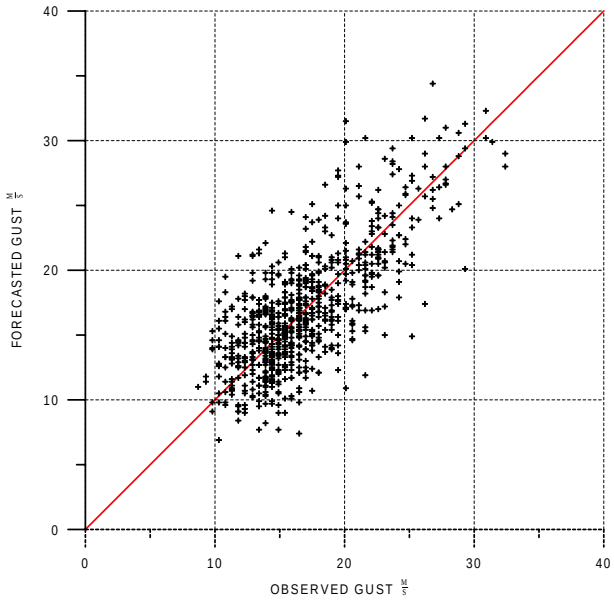

Figure 30: Predicted 10 m wind gust G_u from the similarity method (equation (14)) versus observed 10 m wind gust. Observations are from Danish synop stations in year 2000 (see Tables 1 and 2).

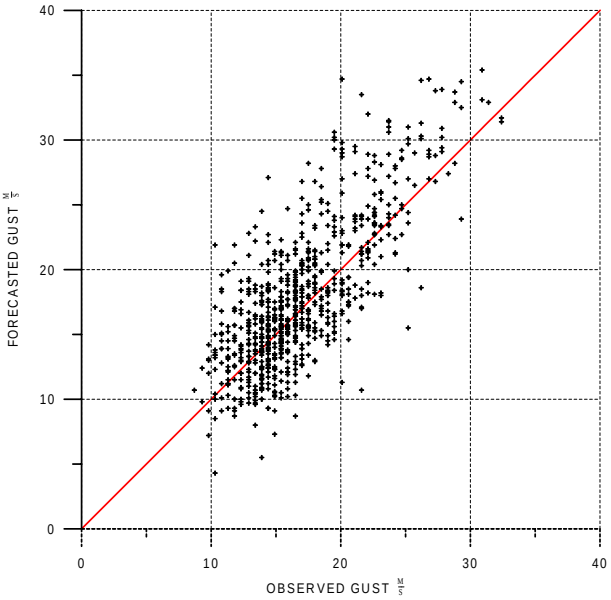

Figure 31: Predicted 10 m wind gust W_g from the TKE-method (equation (30)) (Brasseur, 2001) versus observed 10 m wind gust. Observations are from Danish synop stations in year 2000 (see Tables 1 and 2).

7. Discussion and conclusions

A gust factor formula based on surface layer similarity (the similarity-method) has been developed. The formula has been tested (in a qualitative sense) against observations at an off-shore wind mill farm in the North Sea (Horns Rev) on a day (3 December 1999) with record high wind speeds at the North Sea coast of Jutland. For year 2000 predictions (3 and 6 hours from 00 and 12 UTC) of wind gust and gust factor by the similarity-method have been validated against observations at a number of Danish synop stations. Equally good results are obtained for cases with stable and unstable surface layer stability, although the result for the unstable class is less certain, because of the low number of observations in this class. A similar, but less detailed, validation has been made for an alternative and conceptually different method based on TKE (the TKE-method). Both methods give comparable results, but with a tendency for the TKE-method to predict too high wind gusts, in particular at high gust speeds.

The similarity-method predicts wind gusts with an accuracy similar to the accuracy of the predicted wind speeds.

In a case study (3 December 1999) the major part of the predicted variability in the gust factor over sea, calculated by the similarity-method, is shown to be due to variation in surface layer stability. Only a minor part of the variation is due to variation in the sea surface roughness length. The resulting relatively large horizontal gradient of the gust factor in the surface frontal zones of the Denmark-cyclone is shown to be in good qualitative agreement with observations from Horns Rev.

The similarity-method has some limitations. Theoretically it is only well justified in a horizontally homogeneous surface layer. However, the presented case study indicates that the method also gives applicable results in cases involving surface fronts with considerable horizontal gradients of both temperature, humidity and wind velocity. It is likely to be a more serious limitation that the method only considers gusts generated by turbulence internally in the ABL. Gusts associated with externally generated turbulence, such as turbulent downdrafts in deep convection, are not taken into account. A successful prediction of the latter wind gusts depends primarily on the ability of the model to predict deep convection and secondarily on how realistic these gusts are parameterized. The latter parameterization is most naturally done in the parameterization scheme for deep convection.

Generalization of the gust factor calculation to include gusts generated in deep convection will be a part of future work on prediction of wind gusts. This work will also involve a reassessment of the value of the adjustment parameter c_t as more observational data becomes available.

Acknowledgment

The authors thank H.S. Christensen, ELTRA, for supplying wind data from Horns Rev.

References

Arya, S. (1977). Suggested revisions to certain boundary layer parameterization schemes used in atmospheric circulation models. *Mon. Wea. Rev.*, 105:215–227.

Brasseur, O. (2001). Development and application of a physical approach to estimating wind gusts. *Mon. Wea. Rev.*, 129:5–25.

Browning, K. (1990). Organization of clouds and precipitation in extratropical cyclones. In *Extratropical Cyclones: The Eric Palmén memorial Volume, C.W.Newton and E.O. Holopainin , Eds. , Amer. Meteor. Soc.*, pages 129–153.

Businger, J. A., Wyngaard, J. C., Izumi, Y., and Bradley, E. F. (1971). Flux-profile relationships in the atmospheric surface layer. *J. Atmos. Sci.*, 28:181–189.

Cuxart, J., Bougeault, P., and Redelsperger, J.-L. (1995). Turbulence closure for a non-hydrostatic model. In *12th AMS symp. on Boundary Layer Turbulence*, pages 409–412.

Deardorff, J. W. (1972). Theoretical expression for the countergradient vertical heat flux. *J. Geophys. Res.*, 77:5900–5904.

Garrat, J. R. (1992). *The Atmospheric Boundary Layer.* Cambridge University Press.

Krayer, W. and Marshall, R. (1992). Gust factors applied to hurricane winds. *Bull. Am. Met. Soc.*, 73:613–617.

Nielsen, N. W. and Amstrup, B. (2001). DMI-HIRLAM verification report for the fourth quater of 2000. Dmi internal rep. no. 01-01, Danish Meteorological Institute.

Panofsky, H. A., Tennekes, H., Lenschow, D. H., and Wyngaard, J. C. (1977). The characteristics of turbulent velocity components in the surface layer under convective conditions. *Bound. Layer Meteor.*, 11:355–362.

Paulson, C. A. (1970). The mathematical representation of wind speed and temperature profiles in the unstable atmospheric surface layer. *J. Appl. Meteor.*, 9:857–861.

Sass, B. H., Nielsen, N. W., Jørgensen, J. U., Amstrup, B., and Kmit, M. (2000). The operational HIRLAM system at DMI. Dmi tech. rep. no. 00-26, Danish Meteorological Institute.

Zilitinkevich, S. and Calanca, P. (2000). An extended similarity theory for the stably stratified atmospheric surface layer. *QJRMS*, 126:1913–1924.

DANISH METEOROLOGICAL INSTITUTE

Scientific Reports

Scientific reports from the Danish Meteorological Institute cover a variety of geophysical fields, i.e. meteorology (including climatology), oceanography, subjects on air and sea pollution, geomagnetism, solar-terrestrial physics, and physics of the middle and upper atmosphere.

Reports in the series within the last five years:

No. 96-1
Poul Frich (co-ordinator), H. Alexandersson, J. Ashcroft, B. Dahlström, G.R. Demarée, A. Drebs, A.F.V. van Engelen, E.J. Førland, I. Hanssen-Bauer, R. Heino, T. Jónsson, K. Jonasson, L. Keegan, P.Ø. Nordli, **T. Schmith**, **P. Steffensen**, H. Tuomenvirta, O.E. Tveito: North Atlantic Climatological Dataset (NACD Version 1) - Final report

No. 96-2
Georg Kjærgaard Andreasen: Daily response of high-latitude current systems to solar wind variations: application of robust multiple regression. Methods on Godhavn magnetometer data

No. 96-3
Jacob Woge Nielsen, Karsten Bolding Kristensen, Lonny Hansen: Extreme sea level highs: a statistical tide gauge data study

No. 96-4
Jens Hesselbjerg Christensen, Ole Bøssing Christensen, Philippe Lopez, Erik van Meijgaard, Michael Botzet: The HIRLAM4 Regional Atmospheric Climate Model

No. 96-5
Xiang-Yu Huang: Horizontal diffusion and filtering in a mesoscale numerical weather prediction model

No. 96-6
Henrik Svensmark and Eigil Friis-Christensen: Variation of cosmic ray flux and global cloud coverage - a missing link in solar-climate relationships

No. 96-7
Jens Havskov Sørensen and Christian Ødum Jensen: A computer system for the management of epidemiological data and prediction of risk and economic consequences during outbreaks of foot-and-mouth disease. CEC AIR Programme. Contract No. AIR3 - CT92-0652

No. 96-8
Jens Havskov Sørensen: Quasi-automatic of input for LINCOM and RIMPUFF, and output conversion. CEC AIR Programme. Contract No. AIR3 - CT92-0652

No. 96-9
Rashpal S. Gill and Hans H. Valeur:
Evaluation of the radarsat imagery for the operational mapping of sea ice around Greenland

No. 96-10
Jens Hesselbjerg Christensen, Bennert Machenhauer, Richard G. Jones, Christoph Schär, Paolo Michele Ruti, Manuel Castro and Guido Visconti:
Validation of present-day regional climate simulations over Europe: LAM simulations with observed boundary conditions

No. 96-11
Niels Larsen, Bjørn Knudsen, Paul Eriksen, Ib Steen Mikkelsen, Signe Bech Andersen and Torben Stockflet Jørgensen: European Stratospheric Monitoring Stations in the Artic: An European contribution to the Network for Detection of Stratospheric Change (NDSC): CEC Environment Programme Contract EV5V-CT93-0333: DMI contribution to the final report

No. 96-12
Niels Larsen: Effects of heterogeneous chemistry on the composition of the stratosphere: CEC Environment Programme Contract EV5V-CT93-0349: DMI contribution to the final report

No. 97-1
E. Friis Christensen og C. Skøtt: Contributions from the International Science Team. The Ørsted Mission - a pre-launch compendium

No. 97-2
Alix Rasmussen, Sissi Kiilsholm, Jens Havskov Sørensen, Ib Steen Mikkelsen: Analysis of tropospheric ozone measurements in Greenland: Contract No. EV5V-CT93-0318 (DG 12 DTEE): DMI' s contribution to CEC Final Report Arctic Trophospheric Ozone Chemistry ARCTOC

No. 97-3
Peter Thejll: A search for effects of external events on terrestrial atmospheric pressure: cosmic rays

No. 97-4
Peter Thejll: A search for effects of external events on terrestrial atmospheric pressure: sector boundary crossings

No. 97-5
Knud Lassen: Twentieth century retreat of sea-ice in the Greenland Sea

No. 98-1
Niels Woetman Nielsen, Bjarne Amstrup, Jess U. Jørgensen:
HIRLAM 2.5 parallel tests at DMI: sensitivity to type of schemes for turbulence, moist processes and advection

No. 98-2
Per Høeg, Georg Bergeton Larsen, Hans-Henrik Benzon, Stig Syndergaard, Mette Dahl Mortensen: The GPSOS project
Algorithm functional design and analysis of ionosphere, stratosphere and troposphere observations

No. 98-3
Mette Dahl Mortensen, Per Høeg:
Satellite atmosphere profiling retrieval in a nonlinear troposphere
Previously entitled: Limitations induced by Multipath

No. 98-4
Mette Dahl Mortensen, Per Høeg:
Resolution properties in atmospheric profiling with GPS

No. 98-5
R.S. Gill and M. K. Rosengren
Evaluation of the Radarsat imagery for the operational mapping of sea ice around Greenland in 1997

No. 98-6
R.S. Gill, H.H. Valeur, P. Nielsen and K.Q. Hansen: Using ERS SAR images in the operational mapping of sea ice in the Greenland waters: final report for ESA-ESRIN's: pilot projekt no. PP2.PP2.DK2 and 2nd announcement of opportunity for the exploitation of ERS data projekt No. AO2..DK 102

No. 98-7
Per Høeg et al.: GPS Atmosphere profiling methods and error assessments

No. 98-8
H. Svensmark, N. Woetmann Nielsen and A.M. Sempreviva: Large scale soft and hard turbulent states of the atmosphere

No. 98-9
Philippe Lopez, Eigil Kaas and Annette Guldberg: The full particle-in-cell advection scheme in spherical geometry

No. 98-10
H. Svensmark: Influence of cosmic rays on earth's climate

No. 98-11
Peter Thejll and Henrik Svensmark: Notes on the method of normalized multivariate regression

No. 98-12
K. Lassen: Extent of sea ice in the Greenland Sea 1877-1997: an extension of DMI Scientific Report 97-5

No. 98-13
Niels Larsen, Alberto Adriani and Guido Di-Donfrancesco: Microphysical analysis of polar stratospheric clouds observed by lidar at McMurdo, Antarctica

No.98-14
Mette Dahl Mortensen: The back-propagation method for inversion of radio occultation data

No. 98-15
Xiang-Yu Huang: Variational analysis using spatial filters

No. 99-1
Henrik Feddersen: Project on prediction of climate variations on seasonel to interannual timescales (PROVOST) EU contract ENVA4-CT95-0109: DMI contribution to the final report:Statistical analysis and post-processing of uncoupled PROVOST simulations

No. 99-2
Wilhelm May: A time-slice experiment with the ECHAM4 A-GCM at high resolution: the experimental design and the assessment of climate change as compared to a greenhouse gas experiment with ECHAM4/OPYC at low resolution

No. 99-3
Niels Larsen et al.: European stratospheric monitoring stations in the Artic II: CEC Environment and Climate Programme Contract ENV4-CT95-0136. DMI Contributions to the project

No. 99-4
Alexander Baklanov: Parameterisation of the deposition processes and radioactive decay: a review and some preliminary results with the DERMA model

No. 99-5
Mette Dahl Mortensen: Non-linear high resolution inversion of radio occultation data

No. 99-6
Stig Syndergaard: Retrieval analysis and methodologies in atmospheric limb sounding using the GNSS radio occultation technique

No. 99-7
Jun She, Jacob Woge Nielsen: Operational wave forecasts over the Baltic and North Sea

No. 99-8
Henrik Feddersen: Monthly temperature forecasts for Denmark - statistical or dynamical?

No. 99-9
P. Thejll, K. Lassen: Solar forcing of the Northern hemisphere air temperature: new data

No. 99-10
Torben Stockflet Jørgensen, Aksel Walløe Hansen: Comment on " Variation of cosmic ray flux and global coverage - a missing link in solar-climate relationships" by Henrik Svensmark and Eigil Friis-Christensen

No. 99-11
Mette Dahl Meincke: Inversion methods for atmospheric profiling with GPS occultations

No. 99-12
Hans-Henrik Benzon; Laust Olsen; Per Høeg: Simulations of current density measurements with a Faraday Current Meter and a magnetometer

No. 00-01
Per Høeg; G. Leppelmeier: ACE - Atmosphere Climate Experiment

No. 00-02
Per Høeg: FACE-IT: Field-Aligned Current Experiment in the Ionosphere and Thermosphere

No. 00-03
Allan Gross: Surface ozone and tropospheric chemistry with applications to regional air quality modeling. PhD thesis

No. 00-04
Henrik Vedel: Conversion of WGS84 geometric heights to NWP model HIRLAM geopotential heights

No. 00-05
Jérôme Chenevez: Advection experiments with DMI-Hirlam-Tracer

No. 00-06
Niels Larsen: Polar stratospheric clouds microphysical and optical models

No. 00-07
Alix Rasmussen: " Uncertainty of meteorological parameters from DMI-HIRLAM"

No. 00-08
A.L. Morozova: Solar activity and Earth' s weather. Effect of the forced atmospheric transparency changes on the troposphere temperature profile studied with atmospheric models

No. 00-09
Niels Larsen, Bjørn M. Knudsen, Michael Gauss, Giovanni Pitari: Effects from high-speed civil traffic aircraft emissions on polar stratospheric clouds

No. 00-10
Søren Andersen: Evaluation of SSM/I sea ice algorithms for use in the SAF on ocean and sea ice, July 2000

No. 00-11
Claus Petersen, Niels Woetmann Nielsen: Diagnosis of visibility in DMI-HIRLAM

No. 00-12
Erik Buch: A monograph on the physical oceanography of the Greenland waters

No. 00-13
M. Steffensen: Stability indices as indicators of lightning and thunder

No. 00-14
Bjarne Amstrup, Kristian S. Mogensen, Xiang-Yu Huang: Use of GPS observations in an optimum interpolation based data assimilation system

No. 00-15
Mads Hvid Nielsen: Dynamisk beskrivelse og hydrografisk klassifikation af den jyske kyststrøm

No. 00-16
Kristian S. Mogensen, Jess U. Jørgensen, Bjarne Amstrup, Xiaohua Yang and Xiang-Yu Huang: Towards an operational implementation of HIRLAM 3D-VAR at DMI

No. 00-17
Sattler, Kai; Huang, Xiang-Yu: Structure function characteristics for 2 meter temperature and relative humidity in different horizontal resolutions

No. 00-18
Niels Larsen, Ib Steen Mikkelsen, Bjørn M. Knudsen m.fl.: In-situ analysis of aerosols and gases in the polar stratosphere. A contribution to THESEO. Environment and climate research programme. Contract no. ENV4-CT97-0523. Final report

No. 00-19
Amstrup, Bjarne: EUCOS observing system experiments with the DMI HIRLAM optimum interpolation analysis and forecasting system

No. 01-01
V.O. Papitashvili, L.I. Gromova, V.A. Popov, O. Rasmussen, S. Vennerstrøm: Northern polar cap magnetic activity index PCN: Effective area, universal time, seasonal, and solar cycle variations
(In Press)

No. 01-02
M.E. Gorbunov: Radioholographic methods for processing radio occultation data in multipath regions